

Triggered star formation at the borders of the H II region Sh 2-217^{*}

J. Brand¹, F. Massi², A. Zavagno³, L. Deharveng³, and B. Lefloch⁴

¹ INAF - Istituto di Radioastronomia, via P. Gobetti 101, 40129 Bologna, Italy
e-mail: brand@ira.inaf.it

² INAF - Osservatorio Astrofisico di Arcetri, Largo E. Fermi 5, 50125 Florence, Italy

³ Laboratoire d'Astrophysique de Marseille (UMR6110 CNRS & Université de Provence), 38 avenue F. Joliot-Curie, 13388 Marseille Cedex 13, France

⁴ Laboratoire d'Astrophysique de l'Observatoire de Grenoble, 414 rue de la Piscine, BP 53, 38041 Grenoble Cedex 9, France

Received 13 July 2010 / Accepted 11 November 2010

ABSTRACT

Context. This paper is part of our ongoing study of star formation at the borders of Galactic H II regions. In this paper, we report our observations and analysis of Sharpless 217 (Sh 2-217).

Aims. We study the stars and gas in and around H II regions to see if the various physical parameters derived from the data (such as column densities, masses, sizes, and timescales) are consistent with the predictions of a simple model of the collect-and-collapse mechanism. This should indicate whether stars forming in molecular gas at the borders of the H II regions could have been triggered by the expansion of the ionized gas.

Methods. We observed the emission of various molecules and transitions towards Sh 2-217, and obtained both near-infrared photometry in the *H* and *K* bands, and near-infrared images in [Fe II] and H₂ narrow-band filters of the stars in a molecular condensation at the edge of the H II region, where an UC H II region is also located. For the atomic and ionized hydrogen gas, we used literature data.

Results. Several molecular condensations are found on the borders of Sh 2-217 and both behind and in front of the ionized emission. We find signs of star formation (an UC H II region, outflows, and water masers). The masses of the larger molecular condensations, derived from ¹³CO-data, are ≥ 330 –1100 M_{\odot} , while smaller clumps or cores within them have up to several tens of solar masses. The morphology of the atomic and molecular gas associated with Sh 2-217, especially the condensations of molecular gas on its border, and the presence of star forming activity within them, is strongly indicative of it being the result of star formation triggered by the expansion of the ionized region, following the collect-and-collapse scenario. Application of a simple model illustrates that the present radii of both Sh 2-217 and the UC H II region, the masses of the condensations, and the timescales needed to sweep up these amounts of gas and allow massive stars to form in them, are consistent with the model predictions.

Conclusions. We show that it is highly plausible that the expansion of Sh 2-217 has swept-up the ambient interstellar medium, and that it has taken about 4 Myr to reach its present radius. About 1 Myr ago, the most massive gas condensation became unstable and produced a cluster of stars. The most massive of these stars gave rise to the UC H II region, which took about 0.5 Myr to reach its present size.

Key words. stars: formation – ISM: clouds – ISM: individual objects: Sh 2-217

1. Introduction

Massive stars ($\geq 8 M_{\odot}$; spectral types B3 and earlier) have a significant influence on the morphology and chemical evolution of galaxies. During their lifetime, they transfer large amounts of energy and momentum to the interstellar medium (ISM) through stellar winds and supernova explosions, creating and sustaining turbulence. With their large output of UV photons, massive stars ionize the surrounding ISM creating H II regions.

Through these energetic processes, massive stars can destroy their natal environment, thereby inhibiting any further star formation in the same cloud. On the other hand, through some of the same processes they may also trigger the formation of a new generation of stars. Although there are variations (see Deharveng et al. 2005, for a summary) this may happen in basically two ways: radiation-driven implosion (RDI) and “collect-and-collapse” (see Elmegreen 1998, for a review). In the case of RDI, a *pre-existing* molecular cloud is compressed by the shock

front associated with the expansion of an H II region, which may result in the formation of mostly low- or intermediate-mass stars (e.g., Reipurth 1983; Reach et al. 2004; Lee et al. 2005; Valdetaro et al. 2008). In the collect-and-collapse scenario, on the other hand, a dense layer of swept-up molecular material may form between the shock front caused by the supersonic expansion of an H II region and the ionization front that follows it. This layer may become unstable and fragment; from the dense cores formed in this way, new (massive) stars may form (Elmegreen & Lada 1977; Whitworth et al. 1994). The latter process is attractive because it allows the formation of massive stars or clusters.

To investigate whether the collect-and-collapse mechanism is actually at work in the Galaxy, Deharveng et al. (2005) carefully selected 19 H II regions that are particularly favourable for such a study, based on a number of criteria. So far, the collect-and-collapse process has been shown to be in operation at the borders of Sh 2-104 (Deharveng et al. 2003a), RCW 79 (Zavagno et al. 2006), Sh 2-212 (Deharveng et al. 2008), and RCW 120 (Deharveng et al. 2009; Zavagno et al. 2010). Its presence could not be convincingly demonstrated in the case of

^{*} Full Table 7 is only available in electronic form at the CDS via anonymous ftp to cdsarc.u-strasbg.fr (130.79.128.5) or via <http://cdsarc.u-strasbg.fr/viz-bin/qcat?J/A+A/527/A62>

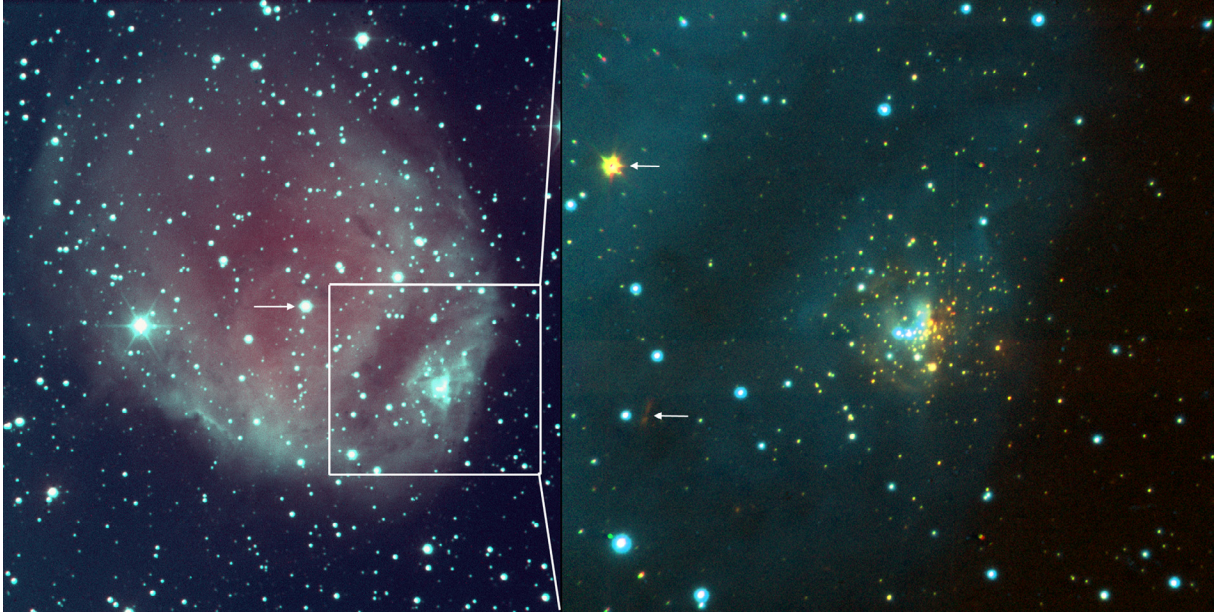


Fig. 1. (Left) **a**) composite colour image of Sh 2-217 in the optical. Pink is for $H\alpha$ (6563 Å), turquoise is for the $[SII]$ emission ($\lambda\lambda$ 6717–6731 Å). The images were obtained with the 120-cm telescope at the Observatoire de Haute Provence (OHP; exposure times 1 h and 2 h, respectively). The field is $\sim 10 \times 11$ arcmin². North is up, east is left. The arrow indicates the exciting star. The box outlines the field seen on the right. (Right) **b**) composite colour image of the cluster on the SW edge of Sh 2-217. Red and green are for the emission in the K - and H -bands, respectively, and blue is for the $H\alpha$ emission. The near-IR frames were obtained at the 3.58-m Telescopio Nazionale Galileo; the $H\alpha$ at the OHP. The top arrow indicates a very red star, which will be discussed in Sect. 4.5; the lower arrow points to a jet/outflow (seen as a reddish streak; see Sects. 4.4 and 4.5).

Sh 2-219 (Deharveng et al. 2006), where the molecular cloud at the edge of the $H II$ region is probably pre-existing rather than swept-up. RCW 82 is also a dubious case: the $H II$ region may be too young to have triggered (by the collect-and-collapse process) the formation of the various YSO's found in the molecular condensations on its border (Pomarès et al. 2009). In this paper, we present the results of our investigation of the $H II$ region Sh 2-217, also taken from the list of Deharveng et al. (2005).

2. Presentation of Sh 2-217

Sh 2-217 (LBN 745) is an optical $H II$ region slightly elongated in the NE–SW direction (Fig. 1a); at the lowest levels of emission, its size is about $560'' \times 450''$, or $11 \text{ pc} \times 9 \text{ pc}$ at a distance of 4.2 kpc (see below). With Galactic coordinates $(l, b) = (159^\circ.17, +3^\circ.33)$, this places the region in the Perseus arm. The main exciting star (ALS8107; Reed 1998) has spectral type O9.5V (Georgelin et al. 1973; Russeil et al. 2007). In the radio-continuum (21-cm; Fig. 2), Sh 2-217 is brightest in a rectangular area centred slightly to the SW of the exciting star with the largest extent in a SE–NW direction, and on the SW-border of the optical emission, where there is an ultra compact (UC) $H II$ region (e.g., Condon et al. 1998). The latter is excited by a (partially embedded) cluster, observed in the NIR by Porras et al. (2000), Deharveng et al. (2003b) and by Leistra et al. (2006). These last authors estimate a lower limit to the age of the cluster of 3 Myr, quite different from the 0.3 Myr age estimated by Porras et al. (2000). Deharveng et al. (2003b) find the earliest type star to be a B0, with ~ 19 mag of visual extinction (assuming the star is on the main sequence).

The UC $H II$ region coincides with IRAS04547+4753 and with a strong (11.6 Jy) resolved ($FWHM 25'' \approx 0.5 \text{ pc}$) point source in the MSX A-band (centred at $8.3 \mu\text{m}$, Egan et al. 1999). Diffuse emission at this wavelength is seen wrapped around the

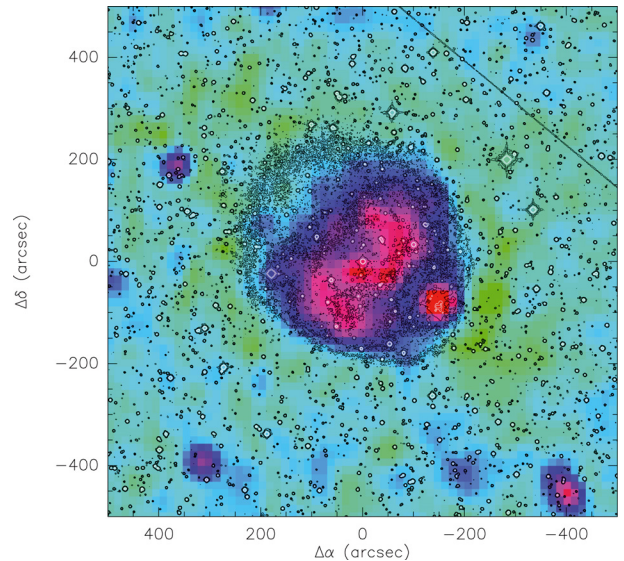


Fig. 2. Sh 2-217. Overlay of 1.4 GHz radio continuum (colour-scale, Condon et al. 1998) and optical (contours; DSS2). The exciting star of Sh 2-217 is at offset (0, 0).

SW border of Sh 2-217, outlining (part of) the photodissociation region (PDR) (see Fig. 2b in Deharveng et al. 2003b).

Moffat et al. (1979) observed a dozen stars in the direction of Sh 2-217. All of these stars are possibly main-sequence stars, at the same distance, and linked to the region. Their visual extinctions are in the range 1.7–3.5 mag. Their star #3 is the exciting star of Sh 2-217 itself. The other stars are located between it and the cluster/UC $H II$ region on the SW-edge of Sh 2-217.

Table 1. Coordinates of objects associated with Sh 2-217.

Source	(J2000)					
	α		δ			
	h	m	s	°	'	''
Exciting star	4	58	45.4	+47	59	55
MSX Sh 2-217	4	58	30.3	+47	58	33
IRAS04547+4753	4	58	29.7	+47	58	28

Deharveng et al. (2003b) discussed the distance determinations for Sh 2-217, finally adopting a distance of 5.0 ± 0.8 kpc. Since then the main exciting star of Sh 2-217 has been reobserved, and the spectral type O9.5V determined by Georgelin et al. (1973) is confirmed by Russeil et al. (2007). In the meantime, new calibrations have become available for O stars (Martins & Plez 2006; Martins et al. 2005). Using these calibrations, a spectral type O9.5V, and the UBV magnitudes measured by Georgelin et al. (1973) and Moffat et al. (1979), we obtain a visual extinction $A_V = 2.11$ mag and a distance $d = 4350$ pc using the B and V magnitudes, and $A_V = 2.37$ mag and $d = 3850$ pc using the U and B magnitudes. Thus, we adopt in the following a distance of 4.2 ± 0.3 kpc for this region. This is roughly consistent with the kinematic distance of 3.5 kpc derived from the observed velocity field (Fig. 2b in Brand & Blitz 1993) for the Galactic longitude of Sh 2-217 and $V_{lsr} = -20$ km s⁻¹.

Sh 2-217 was mapped in H I line emission at 21-cm by Roger & Leahy (1993). They found that the H I emission integrated between ~ -15 and -20 km s⁻¹ almost completely enveloped the optically visible H II region. The mass of the envelope was estimated to be about $510 M_\odot$ (scaled from their distance of 4.7 kpc to 4.2 kpc used here). Jackson & Sewell (1982) mapped a region of $21' \times 11'$ around Sh 2-217 in ¹²CO(1-0) [145 points] with a $1'.1$ beam, and also observed 10 points in ¹³CO(1-0). They derived a mass of the molecular cloud of $\sim 4500 M_\odot$ (scaled to a distance of 4.2 kpc), by extrapolating the ratio $M(\text{H}_2)/T_A^*(\text{CO})$ derived from the positions observed in ¹³CO to the whole cloud. A large region encompassing Sh 2-217, Sh 2-219, and the supernova remnant HB9 was mapped with an $8'.7$ beam by Huang & Thaddeus (1986), who found a total mass for the complex (several degrees in size) of $3.0 \times 10^5 M_\odot$ (scaled to a distance of 4.2 kpc).

Although Sh 2-217 has been studied extensively, observations of the associated molecular gas at sufficiently high resolution have been lacking so far; in the present paper, these are provided. We also present and analyze new data taken in the H and K' broad-band filters, and the H₂ and [Fe II] narrow-band filters, and use more recent 21-cm line and continuum data taken from the archives of the Canadian Galactic Plane Survey. Furthermore, we present single-dish and interferometric observations of water maser emission at various locations in the molecular cloud around the H II region.

In Table 1, we give the coordinates of the exciting star of Sh 2-217 (from Deharveng et al. 2003b) and those of the MSX point source (from Deharveng et al. 2005). The latter coincides to within $6''$ with IRAS04547+4753.

3. Observations and data reduction

3.1. Millimetre-lines

In December 2002, we used HERA (Schuster et al. 2004) at the IRAM 30-m at Pico Veleta (Granada, Spain) to map an area of $17'.6 \times 20'.8$ around Sh 2-217 in ¹²CO(2-1). HERA consists of

Table 2. Details of the molecular line measurements.

Line	Frequency GHz	HPBW ''	B_{eff}^a	F_{eff}^a	rms (res) ^b K (km s ⁻¹)
¹² CO(2-1)	230.537990	12	0.53	0.91	0.56 (0.20)
¹³ CO(1-0)	110.201370	24	0.75	0.95	0.12 (0.11)
¹³ CO(2-1)	220.398686	12	0.55	0.91	0.16 (0.11)
C ¹⁸ O(1-0)	109.782182	25	0.75	0.95	0.13 (0.11)
C ¹⁸ O(2-1)	219.560319	12	0.55	0.91	0.18 (0.11)
CS(2-1)	97.9809680	28	0.77	0.95	0.10 (0.12)
CS(3-2)	146.969049	18	0.69	0.93	0.06 (0.16)
CS(5-4)	244.935557	11	0.50	0.88	0.15 (0.10)
C ³⁴ S(2-1)	96.4129490	28	0.77	0.95	0.06 (0.12)
C ³⁴ S(3-2)	144.617101	19	0.69	0.93	0.06 (0.16)
C ³⁴ S(5-4)	241.016089	11	0.51	0.88	0.14 (0.10)
HCO ⁺ (3-2)	267.557625	10	0.44	0.88	0.15 (0.09)

Notes. ^(a) Beam (B_{eff}) and forward hemisphere (F_{eff}) efficiency. To convert T_A^* antenna temperatures to T_{mb} main beam temperatures, we multiply by $F_{\text{eff}}/B_{\text{eff}}$ (see, e.g., Rohlfs & Wilson 1996, p. 194). ^(b) Average rms in T_A^* , for spectra with the resolution given in brackets.

two receiver arrays of 3×3 pixels with $24''$ spacing. The map was made in on-the-fly (OTF) mode, using the ‘‘coarse sampling’’ option, in which the beam pattern is rotated by $18^\circ.5$. This leads to a slightly under-sampled map, where scan lines (parallel to the right ascension axis) are separated by $7''.6$ in declination.

Based on the map of integrated CO(2-1) emission, we identified three regions for a more detailed study in a variety of molecular lines. These regions represent the more conspicuous local peaks in the CO(2-1) emission (see Fig. 3b). One of them (called Region 1) contains the cluster/UC H II region mentioned in Sect. 2.

Between 2 and 5 July 2003, we used the IRAM 30-m telescope at Pico Veleta to simultaneously observe ¹³CO ($J = 1-0$, $2-1$), C¹⁸O ($J = 1-0$, $2-1$), and CS ($J = 2-1$). A total of 171 positions were observed, mostly on a $12''$ grid. In addition, we simultaneously observed CS ($J = 2-1$, $3-2$, $5-4$) and HCO⁺(3-2) at 16 selected positions (11 in Region 1). The ($J = 2-1$, $3-2$, and $5-4$) transitions of C³⁴S were observed together with HCO⁺(3-2) at 6 of these positions (3 in Region 1). Frequencies, beam sizes, efficiencies, and typical noise levels are given in Table 2.

Observations were mostly carried out in position-switching mode, with the off-position at $(-1200'', -600'')$ with respect to the exciting star (see Table 1), which we used as the reference (0, 0) position in all observations. The observations of C³⁴S were done with a wobbling secondary instead, the wobbler throw being $230''$.

The VESPA auto-correlator backend allowed us to use a variety of resolutions, ranging between 0.09 km s⁻¹ and 0.65 km s⁻¹. In addition we used the 256-channel backend, with 100 kHz filters; this was usually split in two, with each 128-channel section centred on a different transition. At least two different resolutions were used for each transition.

The pointing was regularly checked using a nearby continuum source (NRAO150); receiver alignment was found to be $3''-4''$. The focus was corrected several times during the day by observations of planets (Mars and Saturn), while the line calibration was checked by observations of W3OH.

All data were reduced with the CLASS-package, developed by the Observatoire de Grenoble and IRAM. Low-order polynomial baselines were removed, except for ¹³CO(2-1) and C¹⁸O(2-1), where subtraction of sinusoidal baselines was often necessary.

3.2. Near-Infrared

Near-infrared observations were carried out through H , K' broad-band and $[\text{Fe II}]$, H_2 narrow-band filters with the camera NICS (Baffa et al. 2001) at the 3.58-m Telescopio Nazionale Galileo (TNG; Canary Islands, Spain) on January 4, 2004. The plate scale is $0''.25/\text{pixel}$, yielding a field of view of $\sim 4'.2 \times 4'.2$. The H_2 and $[\text{Fe II}]$ filters are centred on the $2.12 \mu\text{m}$ and $1.64 \mu\text{m}$ lines of H_2 and $[\text{Fe II}]$, respectively. Observing strategy and exposure times are described in Deharveng et al. (2006), the only difference is that the dithering sequence for the H -band images was the same as adopted for K' . The data reduction steps adopted are outlined in Deharveng et al. (2006). Aperture photometry was done using the DAOPHOT (Stetson 1987) package in IRAF. We followed the same procedure described in Deharveng et al. (2006) to obtain aperture photometry, after which PSF-fitting photometry was performed.

Although the seeing was good (less than $1''$), the night was barely photometric, so we calibrated our H , K' photometry with that performed on the same field by Deharveng et al. (2003b). We calculated the difference in magnitudes for each coinciding source and plotted it against our derived instrumental $H - K'$. A colour term was present in K' because of the difference between the K and K' filters. After a best-fit calibration, a residual rms of ~ 0.2 mag was present in the difference between our photometry and that of Deharveng et al. (2003b), probably because of the different seeing and possibly also due to the intrinsic variability of young stars. Our photometry is thus on the same HK standard system as Deharveng et al. (2003b). Sources with $K, H < 11-12$ are in the non-linear regime or saturated, but such bright objects are few in number and lie outside the cluster, and are probably foreground stars. The limiting magnitudes are $K \approx 18.48$ and $H \approx 19.52$, much deeper than achieved by Deharveng et al. (2003b).

Regarding the narrow-band images, we removed the continuum contribution falling in the band by scaling both the narrow-band and the corresponding broad-band frame (K' for H_2 and H for $[\text{Fe II}]$) according to the signal measured for a few stars in the field (which are line-free, pure-continuum sources), and subtracting one from the other. The resulting frame contains only line emission. The flux calibration was obtained by performing aperture photometry (and an aperture correction) on the narrow-band images. We determined the flux of these stars at the filter effective wavelength from the calibrated photometry of the same stars at H and K and derived the linear relation between flux and counts by performing a best fit. For this purpose, H and K magnitudes were converted to fluxes using the zero-magnitude fluxes given by Tokunaga & Vacca (2005). Hence, we found a flux sensitivity limit (at a 3σ level) of $\sim 3 \times 10^{-16} \text{ erg cm}^{-2} \text{ s}^{-1} \text{ arcsec}^{-2}$, in both H_2 and $[\text{Fe II}]$.

The astrometric calibration of the frames was obtained by measuring the position *on the plate* of a sample of stars and fitting those positions to the equatorial coordinates given by Deharveng et al. (2006), using tasks of STSDAS/IRAF. The typical accuracy of this procedure is of the order of $1''$.

3.3. Maser emission

3.3.1. Medicina

We searched for H_2O maser emission with the Medicina 32-m telescope¹ at nine positions in the region of Sh 2-217, between

¹ The Medicina 32-m VLBI radiotelescope is operated by INAF-Istituto di Radioastronomia.

November 2005 and May 2009. We used a bandwidth of 10 MHz and 1024 channels, resulting in a resolution of 9.77 kHz (0.132 km s^{-1}); the HPBW at 22 GHz was $\sim 1'.9$.

The telescope pointing model is typically updated a few times per year, and is quickly checked every few weeks by observing strong maser sources (e.g., W3 OH, Orion-KL, W49 N, Sgr B2, and W51). The pointing accuracy was always better than $25''$; the rms residuals from the pointing model were of the order of $8''-10''$.

Observations were taken in total power mode, with both ON and OFF scans of 5 min duration. The OFF position was taken 1.25° E of the source position to rescan the same path as the ON scan. Typically, three or four ON/OFF pairs were taken at each position, though during some sessions we took 10–14 pairs.

The antenna gain as a function of elevation was determined by observing several times per day the continuum source DR 21 (for which we assume a flux density of 16.4 Jy after scaling the value of 17.04 Jy given by Ott et al. 1994, for the ratio of the source size to the Medicina beam) at a range of elevations. Antenna temperatures were derived from total power measurements in position switching mode. The integration time at each position was 10 s with 400 MHz bandwidth. The zenith system temperature was about 120 K in clear weather conditions.

The daily gain curve was determined by fitting a polynomial curve to the DR 21 data; this was then used to convert antenna temperature to flux density for all spectra taken that day. From the dispersion of the single measurements around the curve, we found the typical calibration uncertainty to be 20%.

3.3.2. Very large array

On 21 April 2008, we used the VLA of the National Radio Astronomy Observatory² (NRAO) in the C-configuration to search for water maser emission at 7 positions in the molecular cloud associated with Sh 2-217. We used a bandwidth of 3.25 MHz with 256 channels of 12.207 kHz (0.1645 km s^{-1}) each. The run was approximately 3 h long and we centred the band at a sky frequency of 22.234824 GHz for all sources. Only right-hand circular polarization was observed. The flux and bandpass calibrator was 3C 48 with an adopted flux density of 1.13 Jy ; the phase calibrator was 0502+416, for which we found a flux density of $0.3055 \pm 0.0045 \text{ Jy}$. Observations of the targets were alternated every 10 min with an observation of the phase calibrator. Each target was observed for a total of 20 min. Pointings on the phase calibrator were made at the start of the observations and approximately half-way during the session.

The data were reduced with the NRAO AIPS software package. The typical rms noise level in the data is $\sim 12 \text{ mJy/beam}$, while the synthesized beam size is $\sim 1''.03 \times 0''.70$. Self-calibration was applied to the strongest source in the sample (Sh 2-217-jet – see Sect. 4.5): the spectral channel with the strongest emission was self-calibrated in amplitude and phase, and the corrections were applied to all channels. Position, velocity, peak flux density, and integrated flux values for each maser spot were derived using the AIPS-task JMFIT.

² The National Radio Astronomy Observatory is operated by Associated Universities, Inc., under contract with the National Science Foundation.

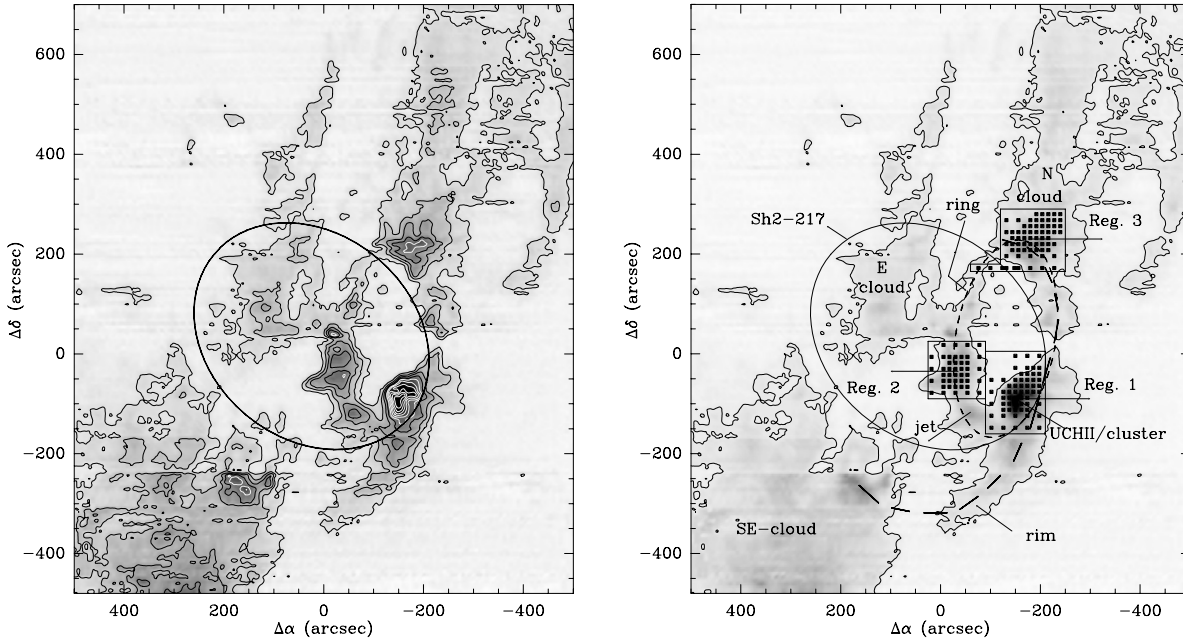


Fig. 3. (Left) **a**) IRAM 30-m, HERA-observations: $^{12}\text{CO}(2-1)$ emission integrated between -23 and -15 km s^{-1} . The exciting star of Sh 2-217, coordinates given in Table 1, is at $(0, 0)$. Contour values are from 10 to 100 K km s^{-1} in steps of 10 K km s^{-1} (levels ≥ 50 K km s^{-1} are drawn in white). The ellipse marks the approximate outline of the optically-visible H II region. The UC H II region is at offset $(-150'', -90'')$ and coincides with the main peak of the CO-emission. (Right) **b**) same as the left-panel, but showing only the 10 K km s^{-1} contour to outline the molecular emission. We have indicated the three regions that were observed in more detail in various molecular tracers (“Reg. 1, 2, 3”; black squares mark observed positions). In projection, these regions appear to form an elliptical structure (marked “ring”; short-dash). Three other structures that are discussed in the text are labeled “N-cloud”, “SE-cloud”, and “E-cloud”. The almost continuous cloud fragment that follows the SW-edge of Sh 2-217, from “Reg. 3” through “Reg. 1” to the CO-peak in the SE-cloud, is labeled “rim” (long-dash). We have also indicated the locations of the jet, the star cluster, and the UCH II region (see text).

4. Results

4.1. Large-scale morphology and kinematic structure

In Fig. 3a, we show the integrated $^{12}\text{CO}(2-1)$ emission. For reference, we delineate the optically-visible H II region. All emission shown lies between $V_{\text{lsr}} = -23$ and -15 km s^{-1} . There is low-level, narrow emission at various velocities outside this range, depending on position, most prominently at about -10 km s^{-1} . The line profile at this velocity is however affected by absorption, which must be due to emission at this velocity at the reference position used for the HERA-observations. The velocity of this component and its occurrence over most of the mapped region suggests that it is due to a nearby cloud and it will not be considered further.

The emission is elongated, generally oriented SE to NW, and has a highly structured morphology. In panel Fig. 3b, we indicated several features that are discussed in the text. There are several regions of enhanced CO-emission seen projected against and at the border of the ionized gas (cf. “Reg. 1, 2, and 3”). Although these regions are not necessarily connected, in projection they appear to form a ring in the SW-part of Sh2 217; for convenience, in the following we refer to this “ring” to indicate the collection of condensations, without implying that it is an entity on its own. An interesting structure is the “rim”, which is the almost continuous cloud filament running along the W-edge of Sh2 217 from the CO-peak labeled “Reg. 3” all the way towards the bright CO spot at the tip of the SE-cloud. The “rim” follows the SW-edge of Sh 2-217 and, as we shall see later, coincides with the photodissociation region (PDR) outlined by the MSX- and H I emission (Fig. 5b).

Channel maps of the $^{12}\text{CO}(2-1)$ emission are shown in Fig. 4. The panels show the emission integrated in intervals of 1 km s^{-1} , centred on the velocity marked in each panel. The strongest emission comes from the “ring”, in particular from Region 1, which coincides in position with the UC H II region/MSX point source. In Table 3, we report the velocity of the peak and the equivalent width ($\int T dv / (1.065 \times T_{\text{peak}})$) of the average emission profile of the various clouds identified in Fig. 3b. The narrowest average profile is found for the E-cloud; it has a $FWHM$ of only 1.7 km s^{-1} ; its line profile has a low-level red-shifted tail. Most average spectra have a non-Gaussian shape. Individual line profiles typically have a Gaussian shape and a $FWHM \sim 1.5$ km s^{-1} . The broad average profiles reflect the presence of velocity gradients across the cloud, as confirmed by Fig. 4. Nearly everywhere the width of the profiles are moreover affected by the presence of multiple emission components (see Sect. 4.3).

The ionized gas has $V_{\text{lsr}}(\text{H}\alpha) \approx -20.4$ km s^{-1} (Fich et al. 1990). This is somewhat blue-shifted with respect to the bulk of the CO-emission, except for the E-cloud. This suggests that if the ionized gas is a “blister”, and participates in a “champagne flow”, the flow axis must be nearly perpendicular to the line-of-sight, as was also concluded by Deharveng et al. (2003b) and Roger & Leahy (1993) before them. If this ionized gas flow existed, the E-cloud could be driven towards us by it. The rest of the molecular gas mapped here would be behind Sh 2-217 as seen from Earth. This prediction is based on the observed velocities, but in the case of the “ring” also on no absorption of the optical H II region being seen where the “ring” is seen across it in projection (cf. Fig. 16). However, a dark band is seen in the SW of Sh 2-217, seemingly separating the UC H II region from

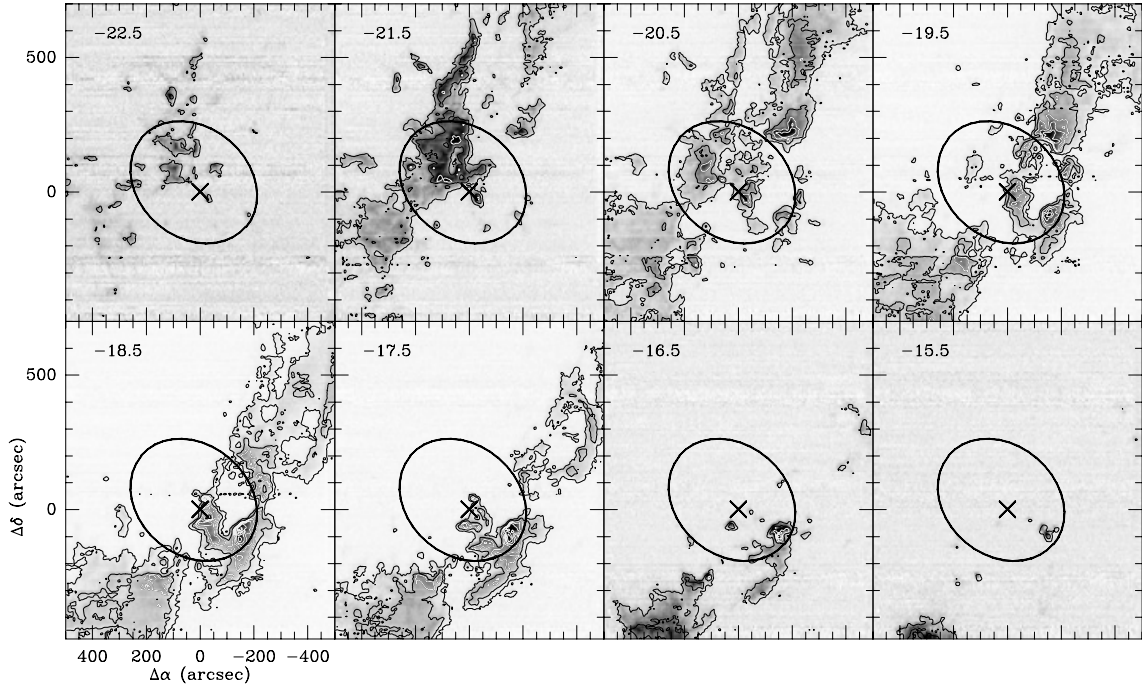


Fig. 4. Channel maps of the $^{12}\text{CO}(2-1)$ emission between -23 and -15 km s^{-1} in steps of 1 km s^{-1} . The central velocity of each panel is given in the upper left-hand corner. Lowest contour 2 K km s^{-1} , step size 4 K km s^{-1} ; contours of 10 K km s^{-1} and higher are white. The cross at offset $(0, 0)$ marks the location of the exciting star of Sh 2-217, while the ellipse shows the outline of the optically-visible H II region.

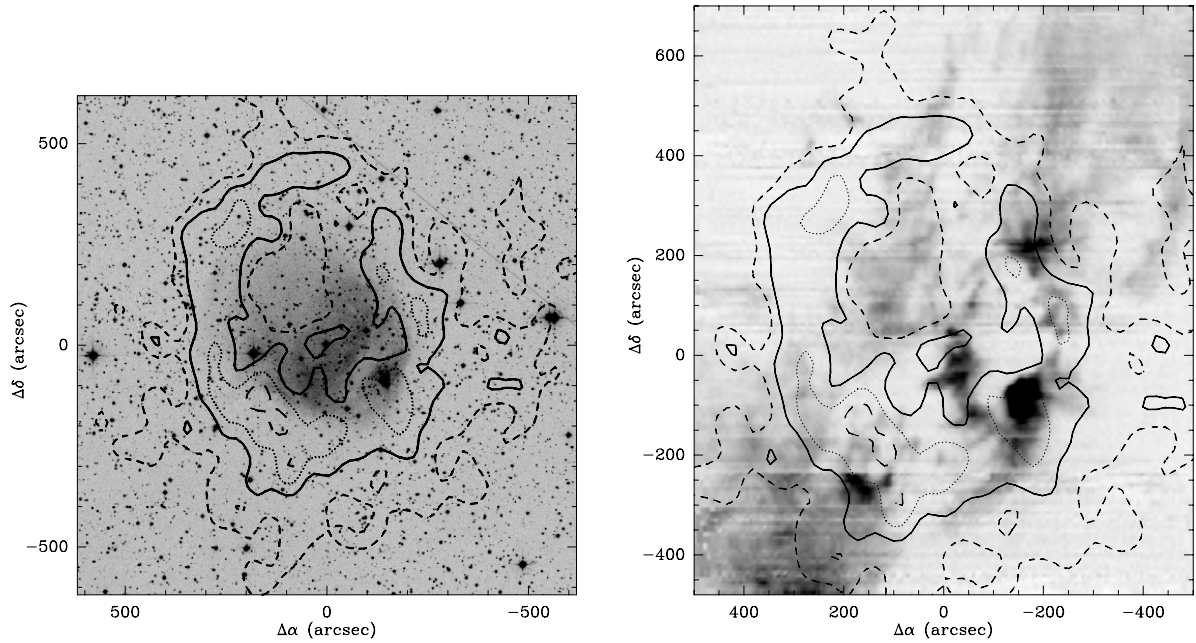


Fig. 5. (Left) **a**) contours of integrated H I line emission ($\int T_b dv$; $V = -22.9$ to -14.7 km s^{-1}) and the optical image of Sh 2-217 (DSS2). Contour values 520 K km s^{-1} (short-dash), 570 K km s^{-1} (continuous), 620 K km s^{-1} (dotted), and 670 K km s^{-1} (long-dash). (Right) **b**) Superimposition of contours of the integrated H I line emission (contours as in left-panel) and a greyscale image of the $^{12}\text{CO}(2-1)$ emission integrated between -23 and -15 km s^{-1} . In both panels, offset $(0, 0)$ as in Fig. 3.

Sh 2-217. This may be caused by atomic hydrogen associated with the region, and lying in front of it (see Sect. 4.2).

We may estimate the total molecular mass as traced by CO , using the empirical relation $N(\text{H}_2) = X \times \int T(\text{CO}) dv$, with $X = 1.9 \times 10^{20} \text{ cm}^{-2} (\text{K km s}^{-1})^{-1}$ (Strong & Mattox 1996). Although this relation was originally found to hold for $^{12}\text{CO}(1-0)$, it is also applicable to $^{12}\text{CO}(2-1)$, assuming that the ratio of the integrals over the $(1-0)$ to $(2-1)$ line profiles is about unity (e.g.,

Brand & Wouterloot 1998). Thus, for the whole molecular complex (i.e., all that is visible in Fig. 3a), we derive a total mass $M(\text{CO}) \approx 1.7 \times 10^4 M_\odot$. Here we considered all spectra with $\int T(\text{CO}) dv > 1$ K km s^{-1} ($\sim 3\sigma$); we did not correct for main beam efficiency, because the CO emission is extended.

Likewise we may derive the masses of the individual clouds making up the complex. The results are collected in Table 3. Calculating virial masses only makes sense for those clouds with

Table 3. Velocity, *FWHM*, and masses of clouds in the Sh 2-217 region.

Cloud ¹	V_{lsr}^2 (km s ⁻¹)	<i>FWHM</i> ³ (km s ⁻¹)	$M(\text{CO})^4$ (M_{\odot})	r_e^5 (pc)
Complex	-18.8	3.8	1.7×10^4	11.1
N-cloud	-19.5	2.8	4.0×10^3	5.5
E-cloud	-21.4	1.7	1.5×10^3	3.3
SE-cloud	-18.9	3.8	6.0×10^3	5.3
Ring	-18.8	3.2	5.8×10^3	–
Reg. 1	-18.3	2.7	1.1×10^3	1.6

Notes. ⁽¹⁾ Clouds are identified in Fig. 3b. ⁽²⁾ Velocity of the peak in the average emission profile. ⁽³⁾ Equivalent width: $\int T dv / (1.065 \times T_{\text{peak}})$. ⁽⁴⁾ From $N(\text{H}_2) = X \times \int T(\text{CO}) dv$; $X = 1.9 \times 10^{20} \text{ cm}^{-2} (\text{K km s}^{-1})^{-1}$. ⁽⁵⁾ $r_e = \sqrt{\text{Area}/\pi}$, and corrected for beam size.

single velocity components. If we assume a density distribution $\propto r^{-2}$, then the virial mass $M_{\text{vir}} = 126 r_e \Delta V^2$ (MacLaren et al. 1988). For the E-cloud, we find $M_{\text{vir}} \approx 1.3 \times 10^3 M_{\odot}$ ($\Delta V \sim 1.8 \text{ km s}^{-1}$).

4.2. Atomic and ionized gas

Emission in the H I line at 21-cm of Sh 2-217 and its surroundings was observed as part of the Canadian Galactic Plane Survey (CGPS, Taylor et al. 2003). The synthesized beam size of the observations is about 1 arcmin ($58'' \times 78''$, at the declination of Sh 2-217). The relevant data file was downloaded from the CGPS-site; the map is in brightness temperature $T_b(\text{K})$.

In Fig. 5, we show the superimposition of the H I line data, integrated between $V_{\text{lsr}} \approx -22.9$ and -14.7 km s^{-1} , and the optical image (Fig. 5a) and the map of integrated CO(2–1) emission (Fig. 5b), respectively. The H I emission was integrated over the same range as the CO-emission. The 21-cm emission at levels above $\int T_b dv \sim 520 \text{ K km s}^{-1}$ forms a closed circular structure, or shell, around the optical H II region, indicating the existence of a photo-dissociated region (PDR) all around it. Peaks in the H I emission are seen at/near locations of intense CO-emission along the “rim”, identified in Fig. 3b, as well as near the CO-peak in the SE-cloud. On the other hand, inside the H I ring there is a lack of 21-cm line emission at the location of the E-cloud (cf. Fig. 3b).

The mean integrated intensity of the 21-cm line emission in the brighter, narrower part of the shell (corresponding roughly to levels above the 550 K km s^{-1} contour) is $\langle \int T_b dv \rangle \approx 585 \text{ K km s}^{-1}$. For optically thin emission ($\tau \ll 1$), the column density of H I is (Rohlfs & Wilson 1996, p. 290) $N(\text{H I}) = 1.82 \times 10^{18} \int T_b dv \approx 1.1 \times 10^{21} \text{ cm}^{-2}$. The area enclosed by the 550 K km s^{-1} contour is $\sim 166 \text{ pc}^2$ at the distance of Sh 2-217. The mass of H I in the shell is therefore $M(\text{H I}) \approx 1.4 \times 10^3 M_{\odot}$.

For the H I-continuum, we used the observations from the VLA-NVVS by Condon et al. (1998). Sh 2-217 was observed with the VLA D-array (synthesized beam size $\sim 44''$). The total integrated flux density is about $264.6 \pm 7.1 \text{ mJy}$, which includes the UC H II region. The UC H II region itself has an integrated flux of $26.6 \pm 2.5 \text{ mJy}$; the total flux density of Sh 2-217 itself is therefore 238 mJy . Using the equations presented in Matsakis et al. (1976), we derive an average electron density of 11 cm^{-3} and 35 cm^{-3} for Sh 2-217 and the UC H II region, respectively. Here we have assumed an electron temperature $T_e = 8000 \text{ K}$. The total number of Lyman continuum photons N_{Lyc} is found to be $\sim 3.60 \times 10^{47} \text{ s}^{-1}$ (Sh 2-217) and $\sim 4.02 \times 10^{46} \text{ s}^{-1}$ (UC H II),

Table 4. Masses¹ of regions² in the Sh 2-217 molecular ring.

Tracer	Region 1 (M_{\odot})	Region 2 (M_{\odot})	Region 3 (M_{\odot})
¹³ CO(1–0)	1100	430	330
C ¹⁸ O(1–0)	310	240	230
CS(2–1)	230–295	135	155

Notes. ⁽¹⁾ Masses for all emission $\geq 3\sigma$ -level, except for ¹³CO where the 3σ -level is outside the observed areas (hence those masses are lower limits). Masses calculated using Eqs. (1) and (2); for abundances, T_{ex} and τ values used, see text. ⁽²⁾ Regions are identified in Fig. 3b.

respectively. Sh 2-217 is excited by a star of spectral type O9.5V (Sect. 2), which has an output of $N_{\text{Lyc}} \sim 1.20 \times 10^{48} \text{ s}^{-1}$ (Panagia 1973). The number of Lyman continuum photons derived from the radio-continuum flux is about 30% of this, implying that most photons are not used for ionisation. These may be absorbed by dust inside the H II region, although in this case it could be because the H II region is density-bounded.

In the UC H II region, the potential exciting stars are two stars of type B2V and at least one star of earlier type (see Deharveng et al. 2003b), perhaps of type B0V (see their Fig. 6). The latter star would have $N_{\text{Lyc}} \sim 4.27 \times 10^{47} \text{ s}^{-1}$; the integrated radio-continuum flux density accounts for only 9.4% of this. In this case, where the ionized region is still embedded in a molecular cloud, this implies that the majority of all photons are absorbed (by dust) in the surrounding medium.

4.3. The molecular ring

In the ¹²CO(2–1) map (see Fig. 3) there are several locations of enhanced ¹²CO intensity, and we have selected three areas (called “Regions” 1, 2, and 3; see Fig. 3b) for a more detailed study in various molecules and transitions (Sect. 3.1 and Table 2). These observations allow us to make a more accurate determination of physical conditions in the molecular gas. In the following, we discuss each region separately.

Column densities N can be derived from optically thin transitions (see, e.g., Rohlfs & Wilson 1996) The excitation temperature T_{ex} is derived, for example, from the optically thick ¹²CO transition. Alternatively, T_{ex} can be derived from the ratio of the C¹⁸O 2–1 to 1–0 line temperatures. If the lines are optically thin, the ratio $R = 4.0e^{-h\nu_{21}/kT_{\text{ex}}}$ (Levreault 1988).

We derive the (LTE) column densities from

$$N_{\text{LTE}} = f(T_{\text{ex}}) \left[\frac{\tau}{1 - e^{-\tau}} \right] \int T_{\text{mb}} dv, \quad (1)$$

where $f(T_{\text{ex}})$ collects the various constants, the partition function, and the frequency of the transition under consideration. In the case of ¹³CO and C¹⁸O, $f(T_{\text{ex}}) = (1.2 \pm 0.2) \times 10^{15} \text{ cm}^{-2} \text{ K km s}^{-1}$ for $T_{\text{ex}} = 5\text{--}20 \text{ K}$ (Kramer 1988; Kramer & Winnewisser 1991). The factor with τ is a correction for optical depth ($\tau < 2$).

The optical depth of ¹³CO and C¹⁸O can be derived from

$$\tau = -\ln \left[1 - \frac{T_A^*}{T_A^*(^{12}\text{CO})} \right], \quad (2)$$

where T_A^* is the antenna temperature of either ¹³CO or C¹⁸O. A summary of the masses derived is given in Table 4. Details and additional information can be found in the text below.

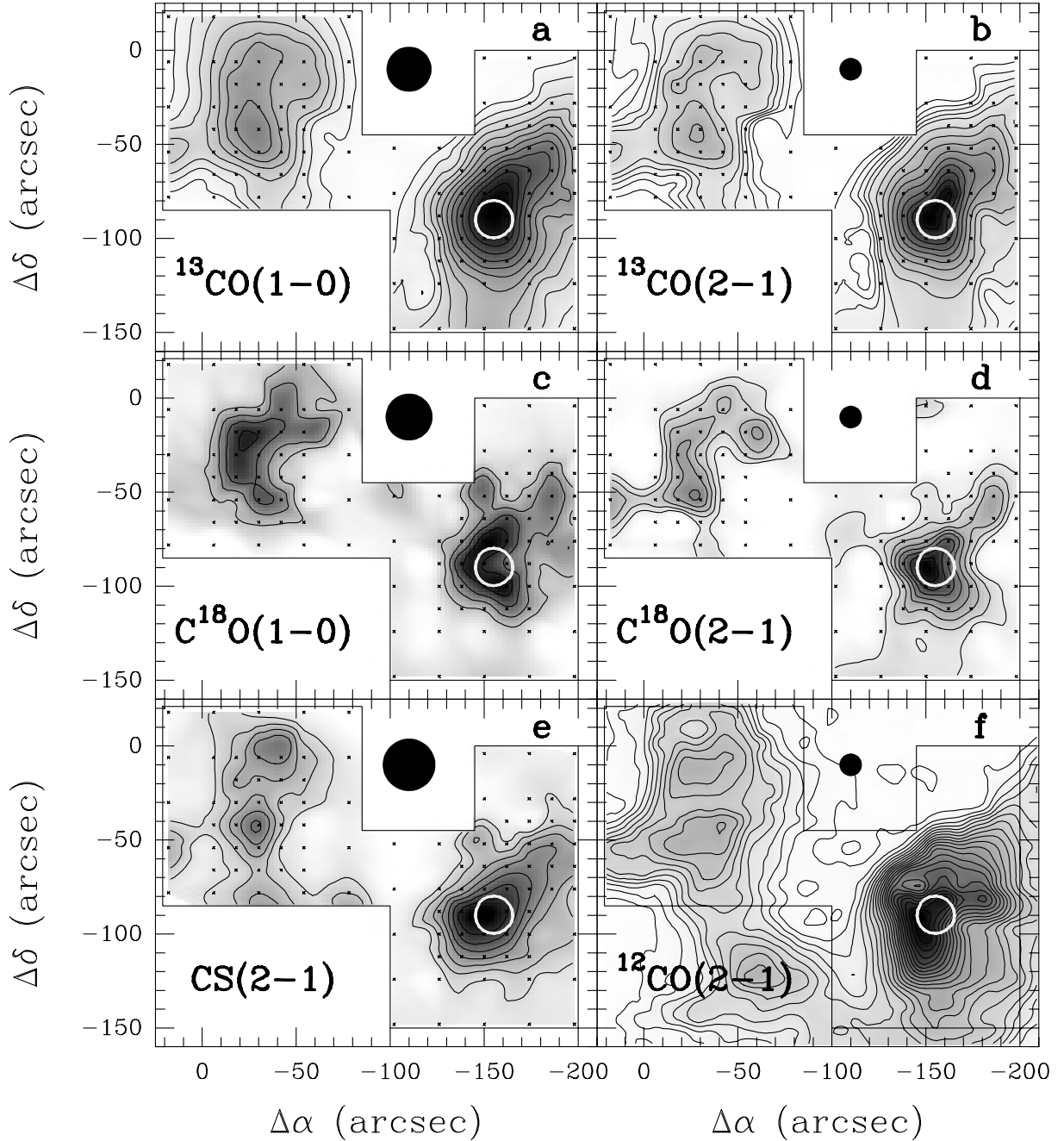


Fig. 6. Emission associated with Regions 1 and 2 (see Fig. 3b). The panels show contours and grey scale of $\int T_{\text{mb}} dv$ (except for $^{12}\text{CO}(2-1)$: $\int T_{\text{A}}^* dv$), where the integration was performed between -23 and -14 km s^{-1} . The molecule and transition are indicated in each panel. The white circle marks the location (but not the size) of the UC H II region and the embedded cluster. The filled black circle marks the beam size. Offset (0, 0) as in Fig. 3. Contour values are in K km s^{-1} and are given below in the format lowest (step) highest. **a)** $^{13}\text{CO}(1-0)$; contours: 2(2)26. **b)** $^{13}\text{CO}(2-1)$; contours: 2(2)10 and 14(4)50. **c)** $\text{C}^{18}\text{O}(1-0)$; contours: 0.5(0.3)1.7. **d)** $\text{C}^{18}\text{O}(2-1)$; contours: 0.9(0.6)6. **e)** $\text{CS}(2-1)$; contours: 0.4(0.25)2.3. **f)** $^{12}\text{CO}(2-1)$; contours 5(5)110.

4.3.1. Region 1

Figure 6 shows a mosaic of plots of the integrated emission associated with Regions 1 and 2 of those molecules/transitions for which complete maps were obtained. For comparison, a map of the integrated $^{12}\text{CO}(2-1)$ emission is also shown.

The sum spectrum of $^{12}\text{CO}(2-1)$ spectra in the same range as covered by the detailed observations, has $T_{\text{A}}^* \approx 20$ K, leading to $T_{\text{ex}} \sim 25$ K. To calculate T_{ex} from the C^{18}O line ratio, we transformed the observed temperatures to T_{mb} , and convolved the (2-1) line profiles to the beam size of the (1-0) observations

at 10 positions in the core of Region 1. The average ratio of the (2-1) to (1-0) lines of ~ 2.3 implies a $T_{\text{ex}} \sim 19$ K. At the *peak* of the molecular emission in this region, line temperatures indicate values of 30–35 K. From these two determinations, it seems that a (conservative) representative value for T_{ex} of Region 1 would be ~ 20 K.

The molecular emission-line profiles in Region 1 can be deconstructed by fitting components at up to three different velocities, although not all are visible in all tracers and not all are visible in each profile of a single tracer. Much of the emission at

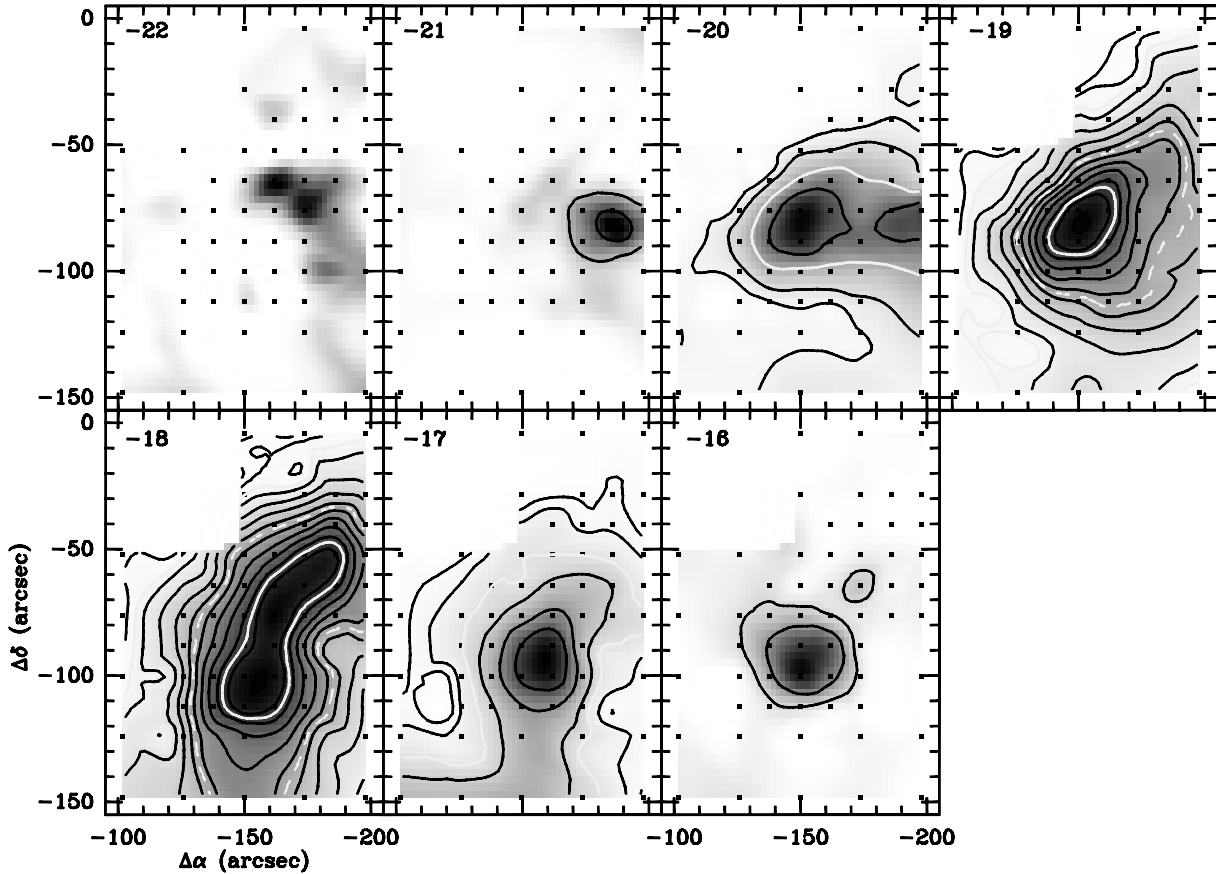


Fig. 7. Channel maps of the $^{13}\text{CO}(1-0)$ emission from Region 1 (see Fig. 3b). Each panel shows the integrated emission in intervals of 1 km s^{-1} centred on the velocity indicated in each panel. Offset (0,0) as in Fig. 3. Black contours: lowest levels 0.25 and 0.5 K km s^{-1} , then in steps of 1 K km s^{-1} . For clarity, full white contours are drawn at levels 1 and 9 K km s^{-1} ; dashed white contour indicates 5 K km s^{-1} .

different velocities peaks at more or less the same positions, as illustrated by the channel maps of $^{13}\text{CO}(1-0)$ shown in Fig. 7.

To estimate the molecular mass detected in the various tracers, we simply consider the bulk of the emission. From the average $^{13}\text{CO}(2-1)$ and $^{12}\text{CO}(2-1)$ spectra in Region 1 and Eq. (2), we find the average ^{13}CO optical depth to be $\langle\tau_{13}\rangle = 0.80$ (peak values are $1.5-1.7$). Likewise, we find that the average C^{18}O optical depth is $\langle\tau_{18}\rangle = 0.03$ (with peak values of $0.05-0.07$).

Applying Eq. (1) to the average integrated $^{13}\text{CO}(1-0)$ emission in Region 1 and assuming an abundance ratio $[\text{H}_2/^{13}\text{CO}] = 5 \times 10^5$ (Dickman & Clemens 1983), we find an average column density of H_2 of $N(\text{H}_2) \approx 1.0 \times 10^{22} \text{ cm}^{-2}$. This results in a total molecular mass, traced by ^{13}CO , of $\sim 1100 M_\odot$, including a correction for He ($\times 1.36$). For $T_{\text{ex}} = 25 \text{ K}$, this mass would be 17% higher.

From the average integrated $\text{C}^{18}\text{O}(1-0)$ emission and an abundance ratio $[\text{H}_2/\text{C}^{18}\text{O}] = 5.9 \times 10^6$ (Frerking et al. 1982), we find an average column density $N(\text{H}_2) \approx 6.1 \times 10^{21} \text{ cm}^{-2}$. The total molecular mass traced by C^{18}O is then $\sim 310 M_\odot$, including a correction for He. For $T_{\text{ex}} = 25 \text{ K}$, this mass would be 17% higher.

We have only a partial map (11 positions) of the UC H II region and the embedded cluster in CS(5-4) and $\text{HCO}^+(3-2)$. The CS(5-4) spectra are rather noisy and the emission is weak, and we determine a mass from the more extensively mapped and stronger CS(2-1) emission. In the case of CS(2-1), the factor $f(T_{\text{ex}})$ in Eq. (1) is (6.3 ± 1.4) for T_{ex} between 5 and 35 K. From Eq. (2) and the C^{34}S data (see below), and assuming a relative abundance $[\text{C}^{32}\text{S}]/[\text{C}^{34}\text{S}] = 22$, we derive a value of $\tau \approx 1.4$ at

the peak. We use $\tau \approx 1$ as a representative value for the entire CS-mapped region. For $T_{\text{ex}} = 20-30 \text{ K}$, the average total (over all velocities) column density of CS above the 0.4 K km s^{-1} (3σ) contour is $N(\text{CS}) \approx (1.0-1.2) \times 10^{13} \text{ cm}^{-2}$. The equivalent beam size-corrected diameter of the area above this level is $\sim 1.7 \text{ pc}$. We then derive a total molecular gas mass, as traced by CS(2-1) of $M \approx (4.6-5.9) \times 10^{-7} [\text{H}_2/\text{CS}]$. With $[\text{CS}/\text{H}_2] = 2 \times 10^{-9}$ (derived for the NGC 2071 star forming region; Zhou et al. 1991), we find a mass of $230-295 M_\odot$ (including a correction for He).

The dominant CS(2-1) emission component is at about -18.5 km s^{-1} . We integrated the emission between -17.3 and -19.3 km s^{-1} to isolate this component. The *FWHM*-contour encloses an area of diameter $\sim 1 \text{ pc}$, and the line width is $\sim 1.5 \text{ km s}^{-1}$. Assuming a density distribution $\rho \propto r^{-2}$, we derive a virial mass $M_{\text{vir}} \approx 140 M_\odot$. The LTE mass within the same *FWHM*-contour ($T_{\text{ex}} = 20-30 \text{ K}$, $\tau = 1$) is $95-105 M_\odot$, comparable to M_{vir} . The situation may be somewhat more complicated, however, as the CS(5-4) data seem to suggest that inside the CS(2-1) *FWHM*-contour there may be at least two smaller cores.

For the -18.5 km s^{-1} component of $\text{HCO}^+(3-2)$, the effective beam size-corrected diameter of the area enclosed by the *FWHM*-contour is $\sim 0.5 \text{ pc}$; the average line width of the emission above the *FWHM* level is $\sim 1.5 \text{ km s}^{-1}$. The virial mass is therefore $\sim 75 M_\odot$. The average total HCO^+ LTE column density for this component, above the *FWHM*-contour, is $1.6 \times 10^{12} \text{ cm}^{-2}$ ($T_{\text{ex}} = 20-30 \text{ K}$). With $[\text{HCO}^+/\text{H}_2] = 2.3 \times 10^{-9}$ (Blake et al. 1987, Orion OMC1-Ridge), this translates into a mass of $3 M_\odot$. This is significantly less than the virial mass, even

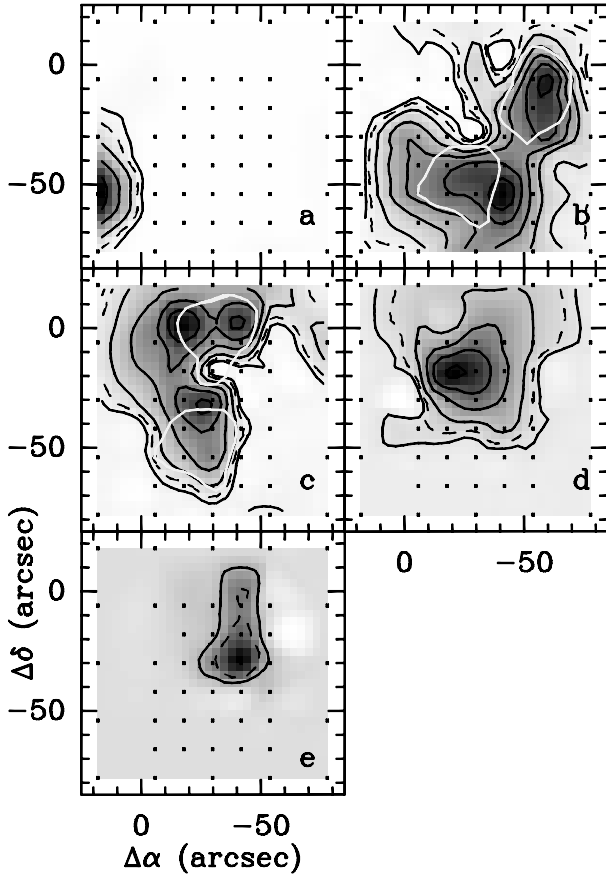


Fig. 8. Maps of $\int T_{\text{mb}} dv$ of the various components contributing to the $^{13}\text{CO}(1-0)$ emission from Region 2 (see Fig. 3b). Each panel shows the integrated emission $\int T_{\text{mb}} dv$ of a single Gaussian component. Offset (0, 0) as in Fig. 3. Black contours: lowest levels 0.5, 1, and 2 K km s^{-1} , then in steps of 2 K km s^{-1} . For clarity, the 1 K km s^{-1} contour is drawn dashed; the white polygons in panels **b**) and **c**) indicate the *FWHM* contours of the corresponding Gaussian component of the CS(2–1) emission (see text and Fig. 10). **a**) Integrated emission of the component between -17 and -18 km s^{-1} . **b**) As a, but for the component between -18 and -19 km s^{-1} . **c**) As a, for the component between -19 and -20 km s^{-1} . **d**) As a, for the component between -20 and -21 km s^{-1} . **e**) As a, for the component between -21 and -22 km s^{-1} .

allowing for the approximate nature of the calculations. In order for the two masses to be comparable, the relative abundance of HCO^+ with respect to H_2 would have to be about 10^{-10} , 25 times lower. Any comparison is hampered by the HCO^+ map being incomplete, and the *FWHM* contour not being closed.

We observed $\text{C}^{34}\text{S}(2-1, 3-2, 5-4)$ at three positions: $(-150'', -88'')$, $(-138'', -88'')$, and $(-174'', -66'')$. The sum of the (2–1) spectra shows a faint 0.07 K (2.8σ) line at -18.52 km s^{-1} , while the (3–2) line was detected at $(-138'', -88'')$ only: $T_{\text{mb}} \sim 0.10 \text{ K}$ (2.4σ) at -18.66 km s^{-1} . The (5–4) transition was undetected.

4.3.2. Region 2

We refer to Fig. 6 for maps of the various tracers that we observed. The emission from Region 2 is complex. The line profiles are the result of the superposition of up to 4 different velocity components. Unlike the situation in Region 1, the various components peak at different locations, as illustrated in Fig. 8, which shows the distribution of integrated $^{13}\text{CO}(1-0)$ emission

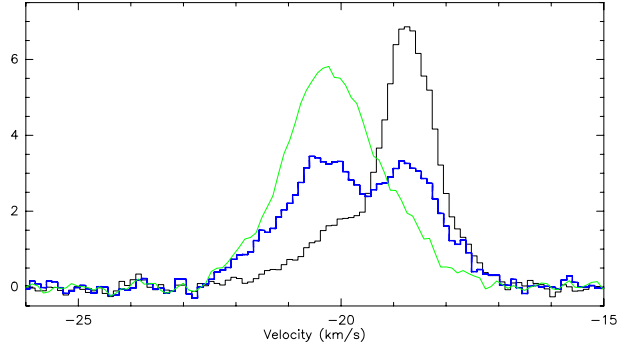


Fig. 9. $^{13}\text{CO}(1-0)$ line profiles from 3 different positions in Region 2 (see Fig. 3b). The black histogram (*right*) shows the emission at offset $(-54'', -18'')$; the green line (*left*) is the profile at $(-30'', -18'')$, while the blue histogram in the middle is at $(-42'', -18'')$.

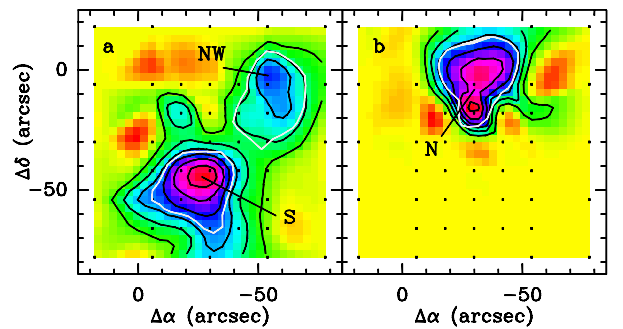


Fig. 10. Maps of $\int T_{\text{mb}} dv$ of the components contributing to the CS(2–1) emission from Region 2 (see Fig. 3b). Each panel shows the integrated emission $\int T_{\text{mb}} dv$ of a single Gauss-fit component. Offset (0, 0) as in Fig. 3. Black contours: lowest level and step 0.2 K km s^{-1} . White contours mark the *FWHM* levels of the three major peaks in the distribution. **a**) Integrated emission of the component at $\sim -18.6 \text{ km s}^{-1}$. **b**) As a, but for the component at $\sim -19.6 \text{ km s}^{-1}$.

for the various Gaussian components fitted to the line profiles. Figure 9 shows three line profiles in a strip at Dec-offset $-18''$.

Both the ratio of the (convolved) $\text{C}^{18}\text{O}(2-1)$ to (1–0) lines and the $^{12}\text{CO}(2-1) T_{\text{A}}^*$ indicate an average value of $T_{\text{ex}} \approx 15 \text{ K}$ for this region. Taking all emission in Region 2 together, and using the same $[\text{H}_2/^{13}\text{CO}]$ and $[\text{H}_2/\text{C}^{18}\text{O}]$ abundances as for Region 1, we find average H_2 column densities $N(\text{H}_2) \approx 5.5 \times 10^{21} \text{ cm}^{-2}$ (^{13}CO , using an average opacity $\langle \tau_{13} \rangle \sim 0.50$) and $4.2 \times 10^{21} \text{ cm}^{-2}$ (C^{18}O ; average $\langle \tau_{18} \rangle \sim 0.05$). Integrating over the whole area where we see emission, we derive molecular masses of 430 and $240 M_{\odot}$ (including a correction for He), from ^{13}CO and C^{18}O data, respectively.

The average total column density of CS(2–1) above the 0.4 K km s^{-1} (3σ) contour ($T_{\text{ex}} = 15 \text{ K}$, $\tau = 1$) is $N(\text{CS}) \approx 5.9 \times 10^{12} \text{ cm}^{-2}$, i.e. $N(\text{H}_2) \approx 3.0 \times 10^{21} \text{ cm}^{-2}$ and $M \approx 135 M_{\odot}$. The line profiles of the higher-density tracer CS(2–1) can be fitted by two Gaussian components, at about -18.6 and -19.6 km s^{-1} . The distribution of $\int T_{\text{mb}} dv$ of both components is shown in Fig. 10. Three clumps/cores are identified by their *FWHM* contours and labeled. The average widths of the CS-line within these contours are 1.55 km s^{-1} (S), 1.11 km s^{-1} (NW), and 1.54 km s^{-1} (N), and the core diameters are $\sim 0.30 \text{ pc}$. We derive virial masses of $M_{\text{vir}} \approx 45 M_{\odot}$ (S), $25 M_{\odot}$ (NW), and $48 M_{\odot}$ (N). These masses are significantly higher than the LTE-masses of the clumps (ca. $4-6 M_{\odot}$). Assuming spherical clumps, these virial masses imply average densities of $3-7 \times 10^4 \text{ cm}^{-3}$. The N-core

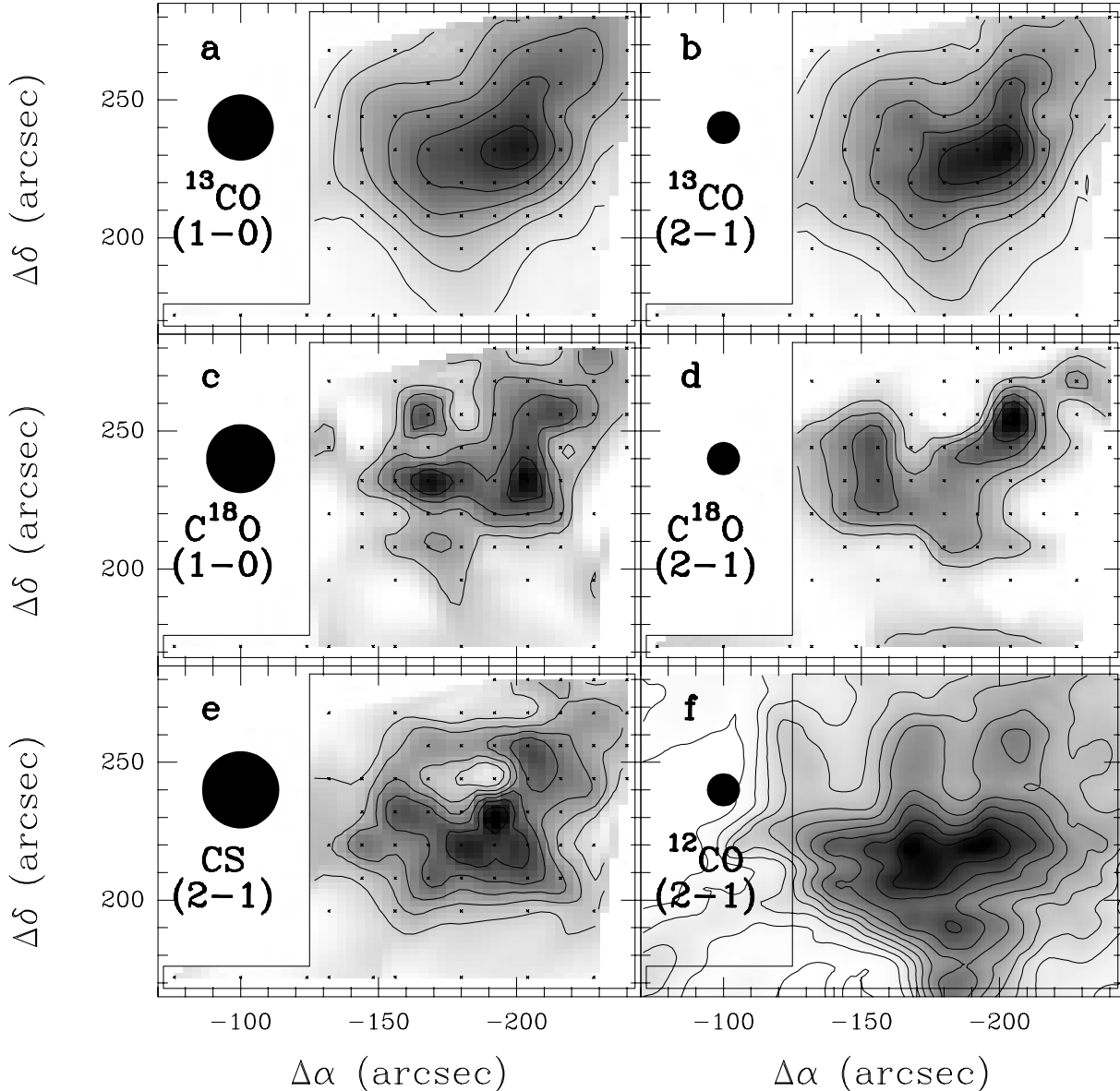


Fig. 11. Emission associated with Region 3 (see Fig. 3b). The panels show contours and grey scale of $\int T_{\text{mb}} dv$ (except for $^{12}\text{CO}(2-1)$: $\int T_{\text{A}}^* dv$), where the integration was performed between -22 and -17 km s^{-1} . The molecule and transition are indicated in each panel. Offset $(0, 0)$ as in Fig. 3. Contour values are in K km s^{-1} and are given below in the format lowest (step) highest. The black circle marks the beam size. **a)** $^{13}\text{CO}(1-0)$; contours: 2(2)14. **b)** $^{13}\text{CO}(2-1)$; contours: 2(2)14. **c)** $\text{C}^{18}\text{O}(1-0)$; contours: 0.4(0.25)1.7. **d)** $\text{C}^{18}\text{O}(2-1)$; contours: 0.6(0.4)2.2. **e)** $\text{CS}(2-1)$; contours: 0.3(0.2)1.7. **f)** $^{12}\text{CO}(2-1)$; contours 5(5)55.

is host to an H_2O maser, which is probably indicative of the presence of a YSO (see Sect. 4.5 and Fig. 20).

The CS clumps are outlined in Fig. 8b,c on the distributions of the integrated emission of the corresponding velocity components in $^{13}\text{CO}(1-0)$. The CS peaks correspond to enhancements in the ^{13}CO distribution; the S-peak in ^{13}CO is also present in the -19 km s^{-1} component (Fig. 8c). The positional coincidence is not perfect: in the N and S-clumps, the ^{13}CO components at ~ -18 and ~ -19 km s^{-1} peak at the edges of, or just outside the CS contour. The C^{18}O emission shows the same effect. This may be due to excitation effects, but it is perhaps more likely to be the consequence of Gaussian fitting leading to slightly different velocities for the components of different molecules.

$\text{HCO}^+(3-2)$ emission was observed and detected at only two positions: at $(-30'', -18'')$ in the N-clump ($T_{\text{mb}} \approx 0.7$ K (3σ) and $\int T_{\text{mb}} dv \approx 0.6$ K km s^{-1} at -19.76 km s^{-1}), and $(-30'', -54'')$ in

the S-clump ($T_{\text{mb}} \approx 0.9$ K (3σ) and $\int T_{\text{mb}} dv \approx 1.3$ K km s^{-1} , at -18.44 km s^{-1}). Assuming $T_{\text{ex}} = 15$ K, we derive column densities of $N(\text{HCO}^+) \approx 3.1 \times 10^{11}$ cm^{-2} and $\approx 6.7 \times 10^{11}$ cm^{-2} for the N and S-clump, respectively.

None of the three C^{34}S transitions were detected at these two positions.

4.3.3. Region 3

We refer to Fig. 11 for a mosaic of plots of the integrated emission associated with Region 3 of molecules/transitions for which complete maps were obtained. For comparison, a map of the integrated $^{12}\text{CO}(2-1)$ emission is also shown.

The line profiles of the various tracers can also here be deconvolved into several components; the components peak at different locations. In Fig. 12, this is shown for $^{13}\text{CO}(1-0)$.

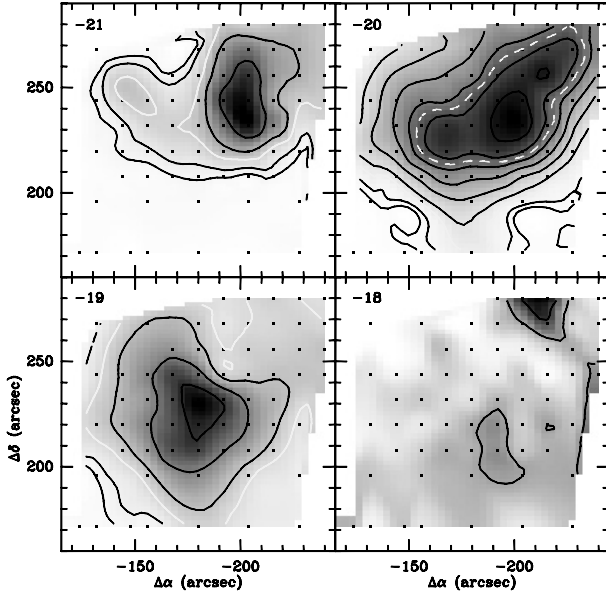


Fig. 12. Channel maps of the $^{13}\text{CO}(1-0)$ emission from Region 3 (see Fig. 3b). Each panel shows the integrated emission in intervals of 1 km s^{-1} centred at the velocity indicated in each panel. Offset (0, 0) as in Fig. 3. Black contours: lowest levels 0.25 and 0.5 K km s^{-1} , then in steps of 1 K km s^{-1} . For clarity, a full white contour is drawn at level 1 K km s^{-1} ; dashed white contour indicates 5 K km s^{-1} .

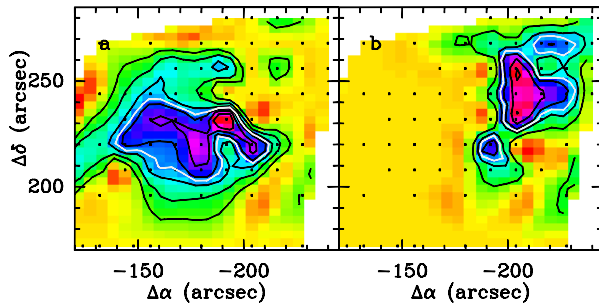


Fig. 13. Maps of $\int T_{\text{mb}} dv$ of the components contributing to the $\text{CS}(2-1)$ emission from Region 3 (see Fig. 3b). Each panel shows the integrated emission $\int T_{\text{mb}} dv$ of a single Gaussian component. Offset (0, 0) as in Fig. 3. Black contours: lowest level and step 0.2 K km s^{-1} . White contours mark the $FWHM$ levels of the three major peaks in the distribution. **a)** Integrated emission of the component at $\sim -19.6 \text{ km s}^{-1}$. **b)** As a, but for the component at $\sim -20.2 \text{ km s}^{-1}$.

From the C^{18}O data, we find that $T_{\text{ex}} \approx 8 \text{ K}$ in this region. The average Region 3 $^{12}\text{CO}(2-1)$ spectrum indicates that $T_{\text{ex}} \approx 17 \text{ K}$. This difference suggests the existence of a temperature gradient, caused by heating from the outside. We adopt $T_{\text{ex}} \approx 10-15 \text{ K}$ as a representative range for this region.

We integrate over all the $^{13}\text{CO}(1-0)$ and $\text{C}^{18}\text{O}(1-0)$ emission and derive average H_2 column densities of $\sim (3.1-3.6) \times 10^{21} \text{ cm}^{-2}$ from ^{13}CO ($\langle \tau_{13} \rangle \approx 0.23$), and $\sim (3.5-4.1) \times 10^{21} \text{ cm}^{-2}$ from C^{18}O ($\langle \tau_{18} \rangle \approx 0.02$). The total molecular mass, including a correction for He, is then $330 M_{\odot}$ (from ^{13}CO) and $230 M_{\odot}$ (from C^{18}O).

From the $\text{CS}(2-1)$ emission above the 3σ level, we derive average column densities of $N(\text{H}_2) \approx 2.5 \times 10^{21} \text{ cm}^{-2}$ ($T_{\text{ex}} = 10-15 \text{ K}$, $\tau = 1$, $[\text{CS}]/[\text{H}_2] = 2 \times 10^{-9}$). This translates into a total LTE mass of $155 M_{\odot}$.

The $\text{CS}(2-1)$ profiles can be fitted by two components. In Fig. 13, we show the distribution of $\int T_{\text{mb}} dv$ for both. We have

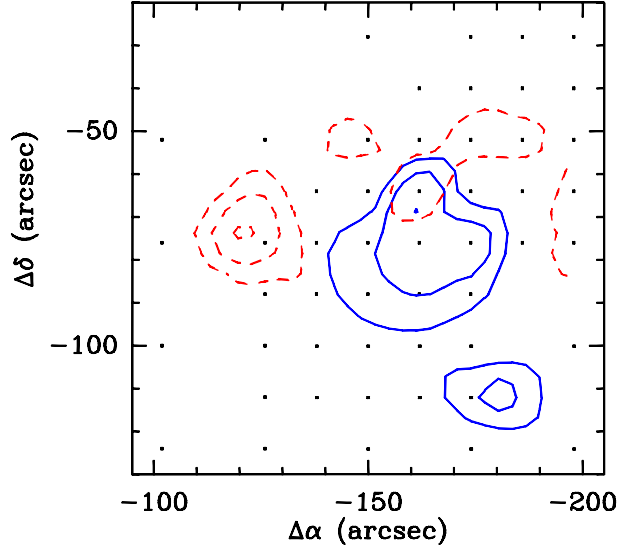


Fig. 14. Outflow emission in cluster region. Offset (0, 0) as in Fig. 3. Blue and red wing emission is shown by the drawn and dashed contours, respectively. We show the integrated $^{13}\text{CO}(1-0)$ emission, after subtraction of the fitted Gaussian components from the line profiles. Blue wing: integrated from -22 to -19.5 km s^{-1} ; red wing: from -17.5 to -15 km s^{-1} . Lowest contour 0.2 K km s^{-1} ($\sim 3\sigma$), step 0.2 K km s^{-1} .

marked the $FWHM$ level (white contours), outlining two major clumps. The average line width of the line profiles inside the $FWHM$ contours is 1.38 km s^{-1} (for the -19 km s^{-1} component) and 1.59 km s^{-1} (for the -20 km s^{-1} component, largest clump). The effective diameters (assuming a circular area and corrected for beam size) are 0.73 pc and 0.32 pc for the -19 km s^{-1} and -20 km s^{-1} components, respectively. This implies virial masses of $M_{\text{vir}} \approx 86 M_{\odot}$ (-19 km s^{-1} component) and $M_{\text{vir}} \approx 49 M_{\odot}$ (-20 km s^{-1} component). Hence, here we also find massive clumps. The corresponding LTE masses (above $FWHM$ -level, $T_{\text{ex}} = 10-15 \text{ K}$, $\tau = 1$, $[\text{CS}]/[\text{H}_2] = 2 \times 10^{-9}$) of these clumps are $30 M_{\odot}$ (-19 km s^{-1} component) and $5 M_{\odot}$ (-20 km s^{-1} component), respectively. The conclusion that these clumps may be unbound is, again, hampered by there appearing to be multiple condensations inside the $FWHM$ -contour, which causes M_{vir} to be overestimated.

$\text{HCO}^+(3-2)$ emission was observed at three positions in this region, and detected only at $(-180'', +220'')$, where we measured $T_{\text{mb}} \sim 1.0 \text{ K}$ (2.4σ) and $\int T_{\text{mb}} dv \sim 0.7 \text{ K km s}^{-1}$, at $V_{\text{lsr}} \sim -19.44 \text{ km s}^{-1}$. For $T_{\text{ex}} = 10-15 \text{ K}$, this translates into a column density $N(\text{HCO}^+) \approx 4.8 \times 10^{11} \text{ cm}^{-2}$. The line was not detected at $(-204'', +220'')$ and $(-192'', +232'')$.

C^{34}S was observed only at $(-192'', +232'')$, where the $(2-1)$ transition was barely detected ($T_{\text{mb}} \sim 0.25 \text{ K}$ (2.6σ) at -19.31 km s^{-1}). The other transitions were not detected.

4.4. Outflow and jet

The line profiles in the three regions discussed above are all superpositions of multiple components, and can be fitted satisfactorily with Gaussians. Only the emission profiles in the embedded cluster region (Region 1) have non-Gaussian wings, indicative of outflowing gas. In Fig. 14, we show the distribution of $\int T_{\text{mb}} dv$ over the wings of the $^{13}\text{CO}(1-0)$ profiles. To identify the wings, we subtracted the fitted Gaussian components from each profile, and integrated the residual emission. The presence of outflows in the embedded cluster, together with the presence

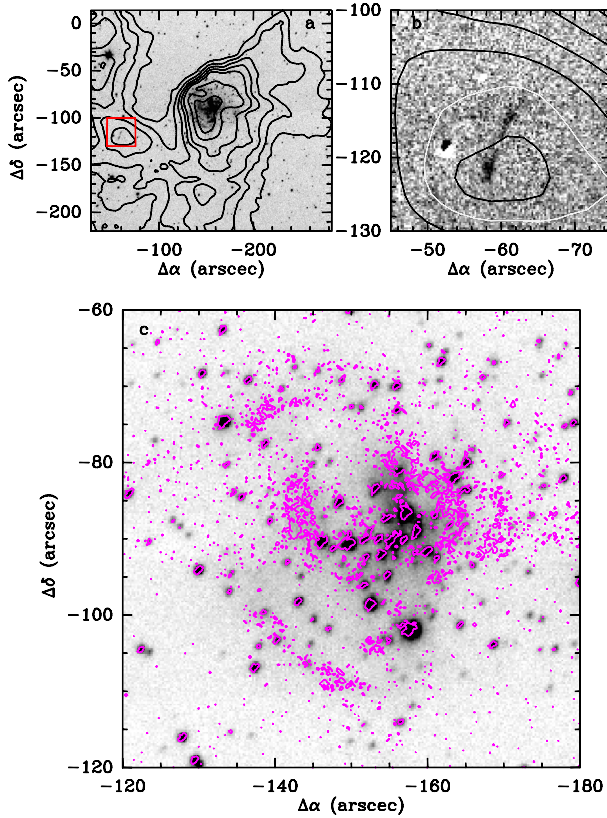


Fig. 15. Region 1 (see Fig. 3b). **a)** H₂-frame (no continuum subtracted) with contours of ¹²CO(2–1) emission integrated between –23 and –15 km s^{–1} (units K km s^{–1}; levels 10 to 50 in steps of 10, then to 110 in steps of 20). The red box (centered on –60′, –115′) indicates the location of a jet-like feature, shown enlarged in the middle panel. **b)** Zoom-in on H₂-jet (continuum-subtracted). Contours of integrated ¹²CO(2–1) emission are shown, in steps of 5 K km s^{–1}; the 40 K km s^{–1} contour is drawn in white. **c)** The cluster region. Grey-scale is the broad-band K′-image. The contours outline the continuum-subtracted narrow-band H₂ emission. In both panels offset (0, 0) as in Fig. 3.

of an UC H II region and H₂O maser emission (see Sect. 4.5) indicate that (massive) star formation is active here. Assuming $T_{\text{ex}} = 20$ K and optically thin emission in the line wings, from the ¹³CO(1–0) data we derive masses of 2.2 and 1.4 M_{\odot} for the blue and red wings, respectively. For $T_{\text{ex}} = 40$ K, the masses would be about 65% higher. Fitting multiple Gaussians to a line profile is a somewhat subjective exercise, and it is easy to mistake outflow emission for separate components. The outflow shown in Fig. 14 is therefore likely to be only “the tip of the iceberg”. The derived masses should therefore be considered as lower limits.

From the narrow-band observations (Sect. 3.2) of the cluster region, we obtained images of the line emission of H₂ and [Fe II]. No [Fe II] emission is detected, but there is diffuse H₂ emission (also after subtraction of continuum) at various locations. These are shown in Fig. 15.

Figure 15a shows the narrow-band H₂ image, before continuum subtraction; Fig. 15b shows a zoom in to the area outlined by the red box in Fig. 15a, revealing what might be an H₂-jet (see also Fig. 1b). The grey scale is the H₂ emission after subtraction of the continuum. We distinguish a northern (N) and a southern (S) part, with H₂ flux densities (uncorrected for extinction) of $(5.8 \pm 0.5) \times 10^{-15}$ erg cm^{–2} s^{–1} (S) and $(6.1 \pm 0.5) \times 10^{-15}$ erg cm^{–2} s^{–1} (N).

In Fig. 15c, we show the broad-band K′-emission (grey-scale) of the cluster area, with the contours of the (continuum-

subtracted) H₂ emission. Several curved filaments are visible. Two brighter ones bracket the cluster to the E and W, while fainter filaments are seen to the NE and SE. This H₂ line emission might be due to fluorescence, or could be shocked gas, created at the location where the outflow(s) from the star formation site(s) impact(s) the ambient gas.

4.5. Water masers

Water maser emission is associated with the very earliest stages of star formation (Codella & Felli 1995; Codella et al. 1996; Furuya et al. 2001, 2003; Breen et al. 2010). With the Medicina 32-m telescope we have searched for water maser emission at nine locations in the region of Sh 2-217. Apart from the central position of the H II region, we targeted the locations of the six massive condensations found in CO (see Fig. 16), towards the centre of the jet seen in H₂-emission (Fig. 15b; cf. Fig. 1b), and towards the location of a peculiar red star (Fig. 1b). Emission was detected clearly towards only three positions (see below). The spectra of all detections are shown in Fig. 17 and the line parameters (from Gaussian fits) are reported in Table 5.

A maser line with a flux density of 2.7–8.3 Jy (>2.5 – 14σ) was detected towards the position of the jet in all but the last of the 11 epochs this position was observed. Maser emission was also detected in Sh 2-217 region 1 (on one occasion out of 15) and in region 2 (on six occasions out of 15). A tentative detection was made towards region 3. In Fig. 18, we show the April 2007 spectrum taken towards this position twice, the one in the lower panel having a resolution of 0.52 km s^{–1} to better bring out the signal. This is an uncertain detection, because the emission is weak, and its velocity differs (by ~ 13 km s^{–1}) from both that of the maser lines at the other three detected positions and that of the CO emission. Nothing was found in three earlier and one subsequent observation towards this location.

The strongest maser signal was thus detected at the position of the jet. As can be seen in Fig. 15b, the jet coincides with a peak in the ¹²CO(2–1) emission (this location was unfortunately not observed in any of the other lines) and the velocity of the CO and the maser are in very good agreement. It is therefore clear that star formation occurs in at least one other location in the molecular gas associated with Sh 2-217, in addition to Region 1, where the presence of the embedded cluster and the UC H II region indicates that star formation has recently occurred. Independently of this, the detection of water maser emission in both Regions 1 and 2 seems to present evidence that star formation is *currently* taking place in at least two of the more massive clumps. However, the observed positions in Regions 1 and 2 are rather close to that of the jet, and there is the possibility that at those positions we detect the maser at the jet-position.

The HPBW of the Medicina telescope at 22 GHz is 1′.9. If we assumed that the beam shape is Gaussian and the maser emission comes only from the jet-position, there having a flux density of 6.5 Jy, then we would expect to find flux densities of 1.0 Jy at Sh 2-217–1, of 2.0 Jy at Sh 2-217–2, and of 1.3 Jy at Sh 2-217–star, respectively. The situation may be more complicated if one takes into account pointing errors, which may increase or decrease the possibility of detecting spill-over emission at any of these positions. The other positions are too distant to detect maser emission originating at the jet-position.

All observations made towards these three positions since June 2007 (date of the first jet-spectrum) are consistent with these flux density values: for the non-detections, the expected spill-over flux density is always less than two times the rms noise

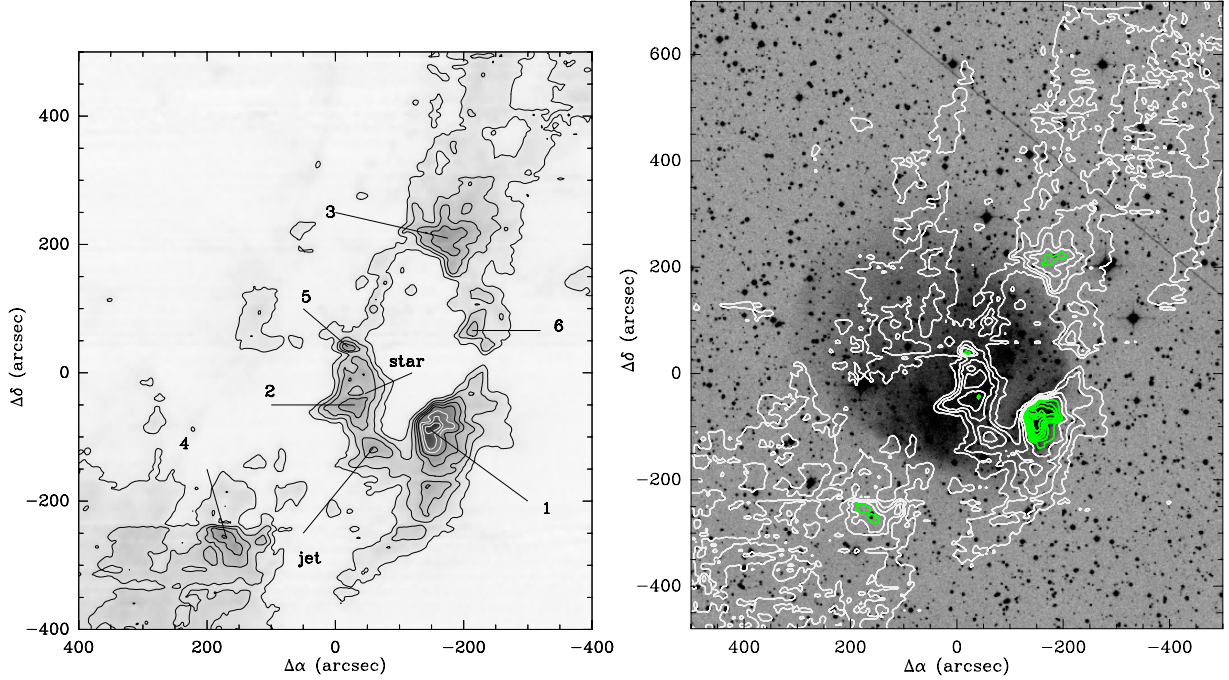


Fig. 16. (Left) $^{12}\text{CO}(2-1)$ emission integrated between -21 and -17 km s^{-1} , showing the molecular “ring”. Contour values are from 10 to 80 K km s^{-1} in steps of 10 K km s^{-1} (the three highest levels are drawn in white). The three most massive clumps defining the “ring” are marked with numbers 1–3; the prominent CO-peak in the SE-cloud is marked with number 4, and minor condensations in the “ring” with 5 and 6. These, as well as “jet” and “star” mark positions towards which we searched for H_2O maser emission (see text). (Right) Overlay of $\int T^{12}\text{CO}(2-1)d\nu$ and optical image. The CO-emission is integrated between -23 and -15 km s^{-1} . Contour values [lowest(step)highest] are 10(10)40 K km s^{-1} (white), 50(10)110 K km s^{-1} (green). In both panels offset (0, 0) as in Fig. 3.

in the spectrum; for the detections (position 2), the emission is 1–2 times the expected spill-over flux density.

However, that in April 2007 we detected a 4 Jy signal at Sh 2-217–1 and nothing in June, while on both dates we detected a ~ 2 Jy line at Sh 2-217–2, does suggest that there is independent maser emission at Sh 2-217–1. This possibility is strengthened by the maser emission detected towards position Sh 2-217–2 being even stronger (3.5 Jy) in February 2007 than in April and June, which implies that if the signal found at Sh 2-217–2 were entirely due to spill-over, there would have been stronger emission (~ 11 Jy) at the jet-position than was detected at any of the other dates. Yet in February no detection was made at Sh 2-217–1. On the basis of presently available observations, we may conclude that independent water maser emission has been detected at the location of the jet, and very likely also at the location of the UC H II region (Sh 2-217–1).

To pinpoint the locations of the maser emission in the region of Sh 2-217, we observed with the VLA in fields centred on Sh-217–1 to 6, and on Sh 2-217–jet (see Sect. 3.3.2). The results are shown in Table 6 and Fig. 19. Emission was found at two positions. At the location Sh 2-217–jet, we distinguish two components: a stronger one at -19.26 km s^{-1} (cf. the Medicina observations) and a weaker one at -13.02 km s^{-1} . The maser emission found at offset $-39''.5$, $-5''.5$ has a different velocity (-25.60 km s^{-1}) than that at the jet position, and was not detected previously at Medicina. It was seen in the field centred on Sh 2-217–2 and that centred on Sh 2-217–5, with slightly different parameters, because the maser location has a different separation from the field center in the two fields. In Table 6, we give the parameters for both detections separately, as well as those for the average spectrum. In Fig. 19, we only show the average spectrum. The maser positions reported in Table 6 were derived using the AIPS-task JMFIT. Spectra around the peak positions

were extracted and Gaussians were fitted to the strongest ones in CLASS, the results of which are also reported in the table. No emission was found at the locations of Sh 2-217–1 and Sh 2-217–2 with the VLA in April 2008, but we note that on the dates immediately before and after nothing was found at these positions with Medicina either. This is likely a consequence of the variable nature of the water maser emission.

The VLA observations locate “VLA-jet” in-between the N and S lobes of the jet seen in H_2 (Fig. 20a). The maser presumably coincides with the driving source of the jet. The maser “VLA-2” coincides with a peak in the $\text{CS}(2-1)$ distribution (Fig. 20b), and in the K' - and H_2 -images its position coincides with a diffuse feature, seen attached to a star. The feature disappears in the continuum-corrected H_2 image.

From these single-dish and interferometric observations we conclude that in the molecular gas seen towards Sh 2-217 there is maser emission at at least three, possibly four different positions. This in turn implies that there is also ongoing star formation in the cloud at locations other than the embedded cluster.

The “peculiar red star” ($\alpha = 04^{\text{h}}58^{\text{m}}40^{\text{s}}.6$, $\delta = +47^{\circ}59'22''$ J2000) towards which we also searched for water maser emission, attracted our attention because it is so much brighter in the NIR than the optical. According to the 2MASS catalogue, $K = 8.29$, $(H - K) = 0.64$, and $(J - H) = 1.62$. These colours are consistent with those of a star of type K–M with visual extinction $A_V \sim 8$ mag. If the object were a main-sequence or giant star, its K -magnitude would require it to be in the foreground – even very nearby (a few tens of parsec) in the case of luminosity class V – which is incompatible with the high extinction. It is more likely to be a background supergiant, unrelated to Sh 2-217 and the cluster.

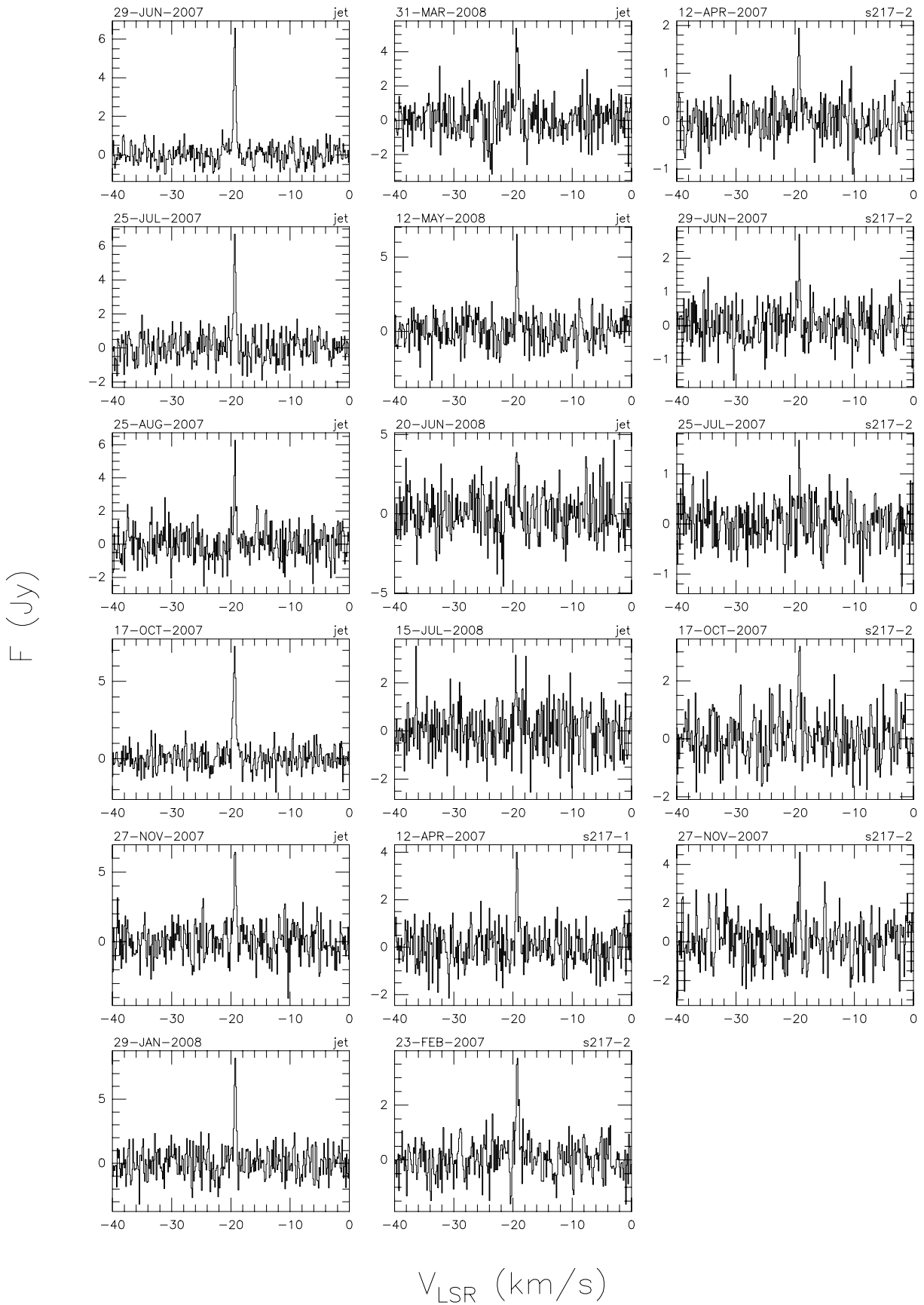


Fig. 17. Spectra of H_2O maser emission towards locations in the molecular material detected towards Sh2 217 (see Fig. 16). The position and observing date are indicated in the upper right- and left-hand corner, respectively, of each spectrum. The resolution is 0.132 km s^{-1} . Only detections are shown.

Table 5. Log of Medicina observations of H₂O masers.

Position ^a	Offset (arcsec)	Date (d/m/y)	rms (Jy)	F (Jy)	Δv (km s ⁻¹)	V_{lsr} (km s ⁻¹)	Position ^a	Offset (arcsec)	Date (d/m/y)	rms (Jy)	F (Jy)	Δv (km s ⁻¹)	V_{lsr} (km s ⁻¹)
Sh 2-217	0, 0	23/11/05	1.17	-	-	-	Sh 2-217-3	-175, +210	12/04/07	0.55	0.80 ^(b)	1.86	-6.49
Sh 2-217-1	-150, -90	23/11/05	0.84	-	-	-			29/06/07	0.52	-	-	-
		30/11/06	1.47	-	-	-	Sh 2-217-4	+170, -256	25/07/07	0.65	-	-	-
		15/01/07	0.86	-	-	-			24/08/07	1.67	-	-	-
		23/02/07	0.72	-	-	-			17/10/07	0.81	-	-	-
		12/04/07	0.82	4.00	0.37	-19.34			28/11/07	1.16	-	-	-
		28/06/07	0.82	-	-	-			31/03/08	1.15	-	-	-
		25/07/07	0.56	-	-	-			12/05/08	1.09	-	-	-
		24/08/07	1.35	-	-	-			20/06/08	1.44	-	-	-
		17/10/07	0.68	-	-	-			15/07/08	0.99	-	-	-
		27/11/07	1.10	-	-	-	Sh 2-217-5	-19, +41	25/07/07	0.51	-	-	-
		29/01/08	1.15	-	-	-			24/08/07	1.82	-	-	-
		31/03/08	1.01	-	-	-			17/10/07	0.91	-	-	-
		12/05/08	1.05	-	-	-			28/11/07	1.15	-	-	-
		20/06/08	1.43	-	-	-			31/03/08	1.38	-	-	-
		15/07/08	0.96	-	-	-			12/05/08	1.12	-	-	-
Sh 2-217-2	-30, -50	23/11/05	0.95	-	-	-			20/06/08	1.54	-	-	-
		30/11/06	1.40	-	-	-			15/07/08	1.15	-	-	-
		15/01/07	0.90	-	-	-	Sh 2-217-6	-214, +66	25/07/07	0.66	-	-	-
		23/02/07	0.56	3.46	0.54	-19.26			17/10/07	0.96	-	-	-
		12/04/07	0.39	1.91	0.39	-19.34			28/11/07	1.33	-	-	-
		29/06/07	0.53	2.45	0.34	-19.31			31/03/08	1.44	-	-	-
		25/07/07	0.40	1.60	0.29	-19.29			12/05/08	1.42	-	-	-
		24/08/07	1.80	-	-	-	Sh 2-217-jet	-59, -117	28/06/07	0.44	6.32	0.45	-19.36
		17/10/07	0.78	3.07	0.50	-19.32			25/07/07	0.73	5.80	0.34	-19.36
		27/11/07	1.13	4.64	0.26	-19.24			25/08/07	0.93	5.57	0.37	-19.32
				3.34 ^(b)	0.25	-14.97			17/10/07	0.68	6.59	0.56	-19.40
		29/01/08	1.23	-	-	-			27/11/07	1.13	6.46	0.46	-19.31
		31/03/08	1.19	-	-	-			29/01/08	1.07	8.27	0.39	-19.27
		12/05/08	1.08	-	-	-			31/03/08	1.00	4.26	0.64	-19.30
		20/06/08	1.42	-	-	-			12/05/08	1.01	6.15	0.33	-19.33
		15/07/08	0.93	-	-	-			20/06/08	1.45	3.78	0.52	-19.37
Sh 2-217-3	-175, +210	23/11/05	1.03	-	-	-			15/07/08	0.98	2.66	0.39	-19.52
		30/11/06	1.40	-	-	-	Sh 2-217-star	-47, -32	02/04/09	1.26	-	-	-
		15/01/07	0.82	-	-	-			28/06/07	0.71	-	-	-

Notes. ^(a) See Fig. 16 for the location in the cloud of the observed positions. Offset (0, 0) is the position of the exciting star of the main H II region. ^(b) Uncertain detection (see text).

Table 6. Results of VLA-C observations of H₂O masers[†].

Field	RA (J2000) Dec						Offset (arcsec)	Date (d/m/y)	rms (Jy)	F (Jy)	Δv (km s ⁻¹)	V_{lsr} (km s ⁻¹)
	h	m	s	°	'	''						
Sh 2-217-jet	04	58	39.47	47	57	57.57	-59.52, -117.43	21/04/08	0.011	3.90	0.52	-19.26
	04	58	39.47	47	57	57.52	-59.52, -117.48	21/04/08	0.011	0.06	1.30	-13.02
Sh 2-217-2	04	58	41.46	47	59	49.48	-39.55, -5.52	21/04/08	0.013	0.41	0.69	-25.64
Sh 2-217-5 ^a	04	58	41.47	47	59	49.52	-39.45, -5.48	21/04/08	0.013	0.63	0.67	-25.57
									0.009	0.51	0.69	-25.60

Notes. ^(†) Positions derived with AIPS-task JMFIT. Line parameters derived from Gaussian fits to the extracted spectra at the peak position. ^(a) Same spot as previous entry, seen in a different field; the last line in the table gives the Gaussian-fit parameters of the average spectrum at this position.

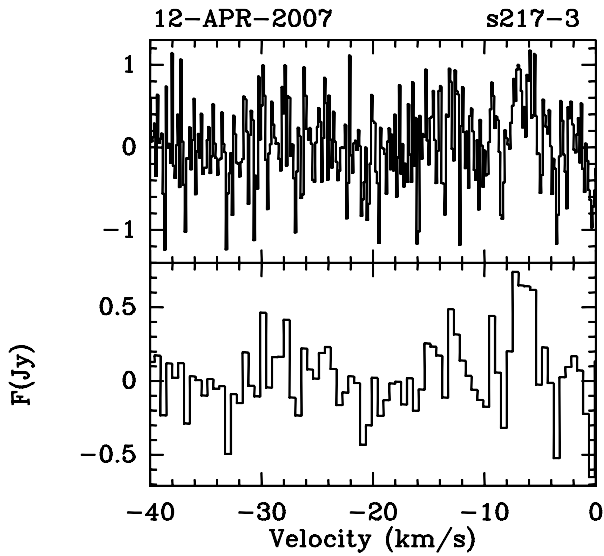


Fig. 18. Spectra of H₂O maser emission towards Sh 2-217-3 (see Fig. 16). The position and observing date are indicated in the upper right- and left-hand corner, respectively. In the top panel, the resolution is 0.132 km s⁻¹. The bottom panel shows the spectrum, smoothed to a resolution of 0.52 km s⁻¹ to better bring out the possible signal. Note that the velocity of the emission differs from that at the other positions, and from that of the CO.

4.6. Stellar component: the cluster

We estimated completeness limits of $K \sim 16.5$ and $H \sim 17.5$ from the peak in histograms of the number of detected sources as a function of magnitude, after binning in 1-mag intervals. A total of 646 NIR sources were detected in both the H - and K -band, and 166 were detected in only one band, within a $\sim 4 \times 4$ arcmin² field. A table with the photometric data is available at the CDS in Strasbourg (see footnote on the title page). A sample is given in Table 7. Columns 1 and 2 list the equatorial coordinates of the stars; Cols. 3 and 4 give the K -magnitude and its error; Cols. 5 and 6 show the H -magnitude and its error, while Cols. 7 and 8 present the derived colour $H - K$ and its error, respectively.

A colour-magnitude (K versus $H - K$) diagram including all sources with a valid detection in both bands is shown in Fig. 21. Most of the stars fall in a strip within $A_V \sim 10$ mag from the ZAMS, but many others lie to the right of this, exhibiting a larger extinction (and, possibly, a NIR excess) up to $A_V \sim 20$ mag. This confirms what was found by Deharveng et al. (2003b). Similar results were obtained by Leistra et al. (2006), who performed JHK photometry quoting roughly the same limiting magnitudes as ours. We have labeled in Fig. 21 the two brightest stars in the

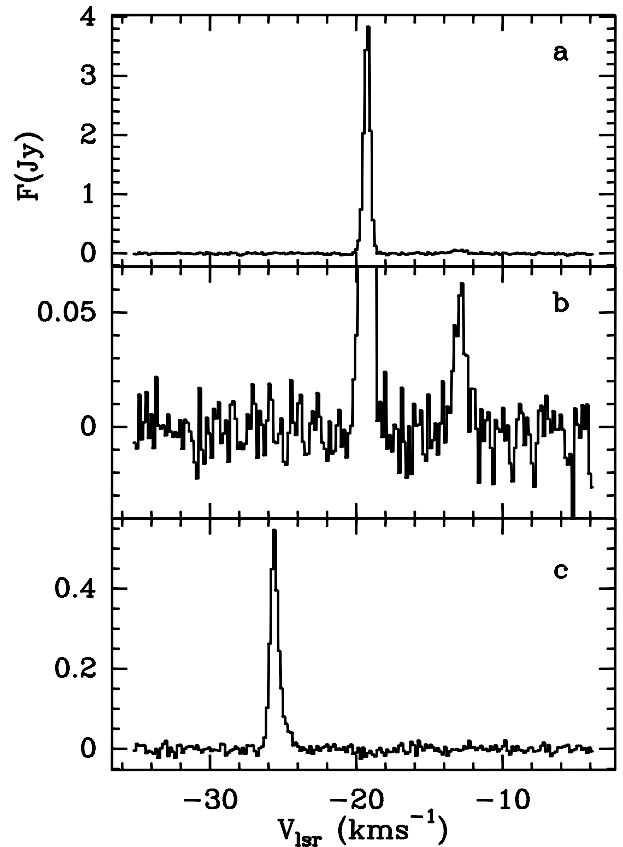


Fig. 19. Spectra of H₂O maser emission obtained with the VLA. **a)** Spectrum of the main emission component at the position of the jet (see Table 6). **b)** As **a)**, but for the secondary component at the jet position. **c)** Spectrum at offset $-39'5, -5'5$. This is the average of the spectrum seen in the observations centred at positions 2 and 5, respectively (see Fig. 16).

cluster (# 32 and # 49, according to the nomenclature adopted by Deharveng et al. 2003b).

If these stars belong to the cluster, they are the most massive members, apparently earlier than B0, although their mass might be overestimated because they are likely to exhibit a NIR excess. Unfortunately, this kind of diagram does not allow us to constrain the age of the cluster. Clues on this issue are suggested by Leistra et al. (2006), who also used deep J images; although they did not present a colour-colour diagram, they note that sources with a NIR excess are few in number. They convert K magnitudes into mass by using a mass-luminosity relation for ZAMS stars. By comparing four embedded young clusters, they conclude that the Sh 2-217 cluster is likely to be older

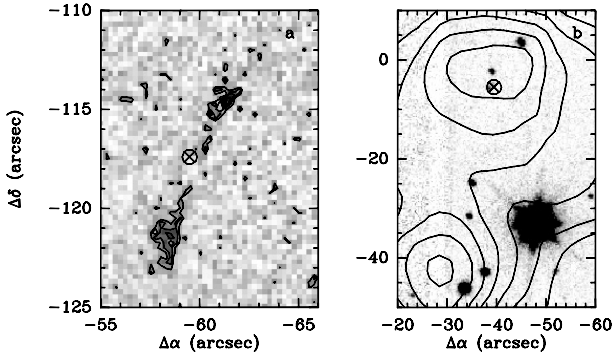


Fig. 20. Location of the VLA H₂O masers. Positions indicated by a crossed circle. Offset (0, 0) as in Fig. 3. **a)** Location of the maser “VLA-jet”. Grey scale shows the continuum-subtracted H₂ emission. **b)** As **a)**, but for the “VLA-2” position. Grey scale shows the K’-image. Contours are shown for the CS(2–1) emission; lowest contour and step 0.2 K km s⁻¹.

Table 7. NIR photometry data (sample; full table available at the CDS).

$\alpha(2000)$ h m s	$\delta(2000)$ ° ' "	K	σ_K	H	σ_H	$H-K$	σ_{H-K}
4 58 42.00	47 56 22.16	17.502	0.097	18.389	0.112	0.887	0.148
4 58 41.46	47 56 33.29	17.796	0.131	18.561	0.076	0.765	0.151
4 58 27.79	47 56 34.86	15.821	0.025	16.010	0.029	0.189	0.038
4 58 28.23	47 56 35.67	16.621	0.037	16.861	0.033	0.240	0.050
4 58 26.90	47 56 39.44	15.339	0.022	15.731	0.026	0.392	0.034
4 58 41.57	47 56 48.88	15.315	0.059	16.462	0.078	1.148	0.098
4 58 25.99	47 56 52.65	16.914	0.059	17.352	0.030	0.438	0.066
4 58 30.00	47 56 57.07	17.741	0.087	18.247	0.042	0.507	0.097
4 58 20.67	47 56 57.32	17.387	0.065	17.664	0.034	0.277	0.073
4 58 41.79	47 57 00.31	17.109	0.068	18.194	0.080	1.085	0.105
4 58 31.50	47 57 00.61	16.283	0.027	16.726	0.024	0.443	0.036
4 58 27.71	47 57 02.82	13.575	0.011	13.752	0.012	0.177	0.016
4 58 20.50	47 57 05.44	17.541	0.079	17.914	0.048	0.373	0.092
4 58 22.44	47 57 09.53	14.571	0.024	14.743	0.018	0.173	0.030
4 58 28.05	47 57 11.34	17.206	0.069	17.500	0.035	0.294	0.077
4 58 19.30	47 57 14.04	16.182	0.039	16.073	0.033	-0.109	0.051
4 58 18.18	47 57 14.26	17.757	0.099	17.823	0.057	0.066	0.114
4 58 21.50	47 57 16.28	16.923	0.034	17.152	0.023	0.229	0.041
4 58 29.67	47 57 16.79	15.404	0.016	15.609	0.019	0.205	0.025
4 58 21.94	47 57 17.29	15.739	0.023	15.910	0.015	0.171	0.027
4 58 27.37	47 57 21.53	17.306	0.069	17.648	0.031	0.342	0.076
4 58 30.11	47 57 25.58	16.315	0.033	16.650	0.029	0.335	0.044
4 58 27.89	47 57 28.91	15.022	0.014	15.198	0.015	0.176	0.021
4 58 25.82	47 57 30.50	16.508	0.029	16.982	0.024	0.474	0.038
4 58 26.74	47 57 36.12	16.951	0.049	17.188	0.034	0.238	0.060

than 3 Myr. This is however at odds with the age of 0.3 Myr obtained by Porras et al. (2000). Both age constraints are uncertain. On the one hand, Leistra et al. (2006) estimate the age of *another* cluster in their sample from the fraction of member stars with NIR-excess (60–80%) to be “less than 3 Myr”; because the other clusters, including Sh 2-217, have less nebular emission and have fewer stars with a NIR-excess, the conclusion is that they are older. However, from Hillenbrand (2008; Fig. 3a) one would derive an age less than about 1 Myr for a cluster with 60–80% of stars with $H - K$ colour excess. On the other hand, Porras et al. (2000) derive a J -luminosity function (JLF) for the cluster, and compare it with theoretical ones obtained by assuming a standard IMF and a set of pre-main sequence (PMS) evolutionary (age) tracks. However, by using the J -band, many reddened members may not be detected. Furthermore, these authors

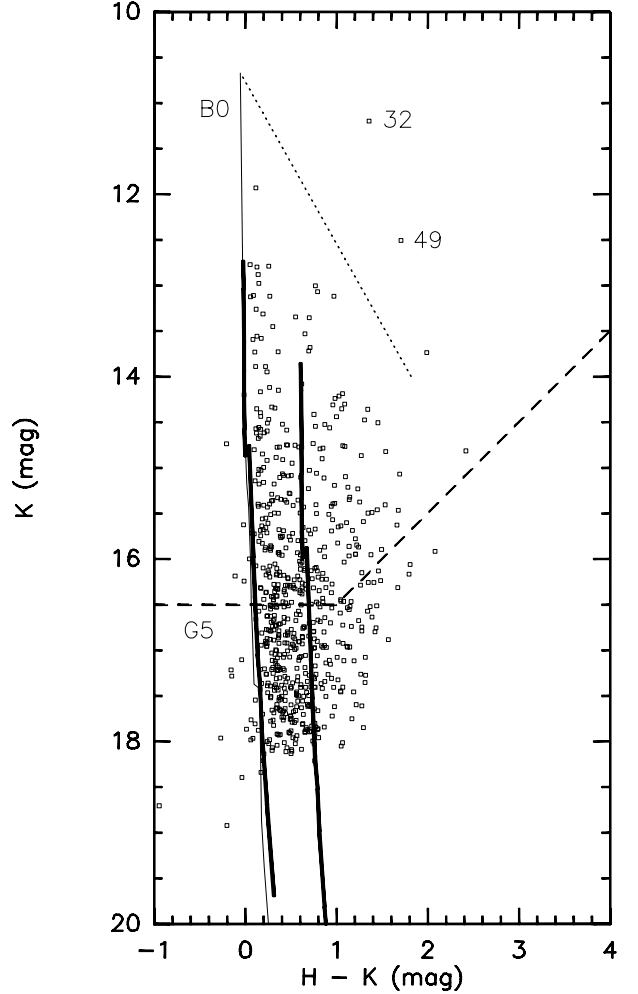


Fig. 21. K versus $H - K$ for all sources with detections in both bands (open squares). The dashed lines mark the completeness limit, whereas the thin line is the locus of the ZAMS (absolute magnitudes from Allen 1976, colours from Koornneef 1983) for the distance of Sh 2-217 (4.2 kpc). The dotted line indicates the reddening direction; the length of the line corresponds to an extinction of $A_V = 30$ mag. The adopted extinction law is from Rieke & Lebofsky (1985). The thick lines are isochrones for PMS stars 1 Myr old (with $A_V = 0$ and 10 mag, left to right) ranging from 0.1 to 6 M_\odot (from Palla & Stahler 1999). Labeled are the two brightest stars towards the cluster, following the nomenclature adopted by Deharveng et al. (2003b).

then derive an IMF for the cluster that is flatter than the one used to construct the theoretical JLF.

Porras et al. (2000) also present a colour-colour diagram for the cluster field (see their Fig. 1), with a large number of sources exhibiting a ($H - K$) NIR excess (they estimate a fraction of Herbig Ae/Be plus classical T Tauri stars of 65%). From Hillenbrand (2008; Fig. 3a), we see that this, too, implies an age ~ 1 Myr.

To better outline the cluster morphology, we have mapped the stellar surface density by counting all sources (above the completeness limit) in $20'' \times 20''$ squares, the centres of which are displaced from one another by $10''$ in right ascension or declination. The result is shown in Fig. 22a. We have also plotted the locations of the sources with $H - K > 1$ (filled squares). The cluster appears slightly smaller and more compact than that seen towards Sh 2-219 (Deharveng et al. 2006). The reddened sources clearly cluster towards the surface-density peak, while

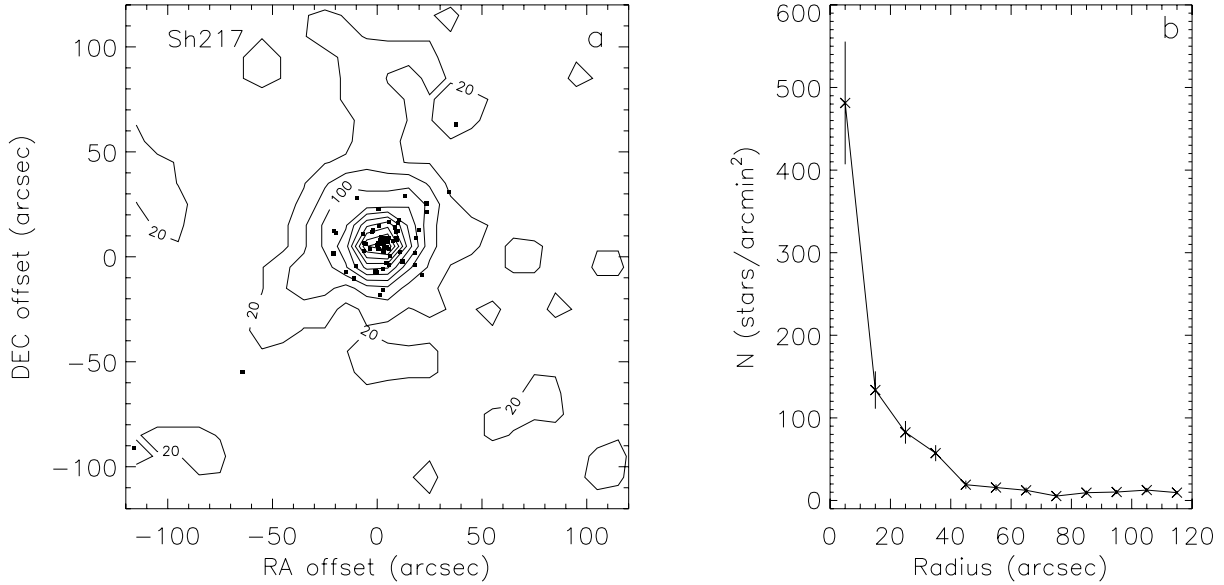


Fig. 22. **a)** Stellar surface density distribution (stars arcmin⁻²); coordinates are arcsec offsets from the density peak at RA(2000) = 4:58:30.0 Dec(2000) = +47:58:20. Filled small squares mark the positions of sources with $H - K > 1$. **b)** Radial density distribution (stars arcmin⁻²) centred on the peak of the stellar surface density.

in the Sh 2-219 cluster the reddened source distribution appears to be elongated along the ionization front. This might also suggest that the Sh 2-217 cluster is younger.

The radial distribution of the stellar surface density was derived by counting all sources (above the completeness limit) in 10''-wide annuli centred on the cluster's centre. The result is shown in Fig. 22b. The plot shows the presence of a compact core of stars within the cluster. This confirms that the cluster is much more compact than the one in Sh 2-219, which has a less sharply-peaked profile (see Fig. 8b in Deharveng et al. 2006). From the radial density distribution of Fig. 22b, we estimated the number of cluster members (down to the completeness limit) following Testi et al. (1997). The cluster size was also derived from the radial density distribution, by taking the radius at which the distribution reaches a constant (background) value (i.e., ~65''). The completeness limit in mass, M_{compl} can be estimated from the completeness limit at K by adopting a set of evolutionary tracks. According to Palla & Stahler (1999), $K = 16.5$ corresponds to a PMS star 10⁶ yrs old of 0.3 M_{\odot} or a PMS star 10⁷ yrs old of 1 M_{\odot} . Adding an $A_V = 10$ mag, these mass limits increase to 0.8 and 1.3 M_{\odot} , respectively. Hence, the cluster population is probably well-sampled down to stars of ~1 M_{\odot} . This means that the number of members down to $K = 16.5$ is a lower limit to the total number of members; assuming an IMF similar to that of Scalo (1998), the correction amounts to a factor of from 2 ($M_{\text{compl}} = 0.4 M_{\odot}$) to 6 ($M_{\text{compl}} = 1 M_{\odot}$), without including unresolved companions and stars below the hydrogen burning limit. However, given the local extinction gradient $E(B - V) = 0.61$ mag kpc⁻¹ (Spitzer 1978), we can estimate $A_V \sim 9.5$ mag for sources at the assumed distance of Sh 2-217. Hence, cluster members with $A_V \sim 0$ mag are quite unlikely and the larger correction factor seems most appropriate.

By using two different methods to correct for extinction, Leistra et al. (2006) derive an IMF for the cluster with a slope Γ in the range -2.7/-1.6 (a Scalo IMF has $\Gamma = -1.7(1-10) M_{\odot}$; -1.3(10-100) M_{\odot}); the lower value is obtained when individual extinction corrections are applied to each star, rather than an average, identical correction for all. Porras et al. (2000) find

Table 8. Cluster parameters.

Number of members with $K < 16.5$	~141
Fraction of members with $H - K > 1$	20 %
Radius	1.3 pc
Expected number of members ^a down to 0.1 M_{\odot}	254 (605)
Expected number of members ^a with $M > 10 M_{\odot}$	1 (3)
Total stellar mass ^a	183 (435) M_{\odot}
Star-formation efficiency ^b	14% (28%)

Notes. ^(a) Assuming all the stars down to 0.3(0.8) M_{\odot} have been detected. ^(b) Defined as $M_*/(M_* + M_{\text{gas}})$; $M_{\text{gas}} = 1100 M_{\odot}$ (Table 4).

$\Gamma \sim -0.59$. This discrepancy may be due to Porras et al. (2000) using only stars in the cluster *core*, which may bias them towards more massive stars (assuming there is mass segregation), resulting in a flatter IMF (Leistra et al. 2006). We can only conclude that at the moment there is no evidence that the Sh 2-217 cluster exhibits an IMF that significantly differs from a standard one, justifying our a priori assumption of a Scalo IMF.

All derived parameters for the cluster are listed in Table 8. Leistra et al. (2006) note that the surface star density they find does not reach a plateau out to as far as 80'' (1.6 pc at 4.2 kpc) from the cluster centre, concluding its radius has to be larger than that. By exploiting a larger field of view than theirs, we instead find a radius of “only” ~65'' (1.3 pc at 4.2 kpc; see also Fig. 22b). On the other hand, the number of cluster members they estimate is fully consistent with our derivation.

5. Discussion and conclusions

On the basis of our data analysis presented here, we can conclude that there is about $1.7 \times 10^4 M_{\odot}$ of molecular material in the $\sim 20 \times 20$ pc² area around the optical H II region Sh 2-217 that we mapped. Based on the relative velocities of the molecular and ionized gas, and signs of their interaction, we believe most of the

molecular gas is associated with the H II region. From the morphology of the $^{12}\text{CO}(2-1)$ emission, we distinguish four major complexes (the SE, E, and N-clouds, and the CO-maxima forming the “ring” and “rim” – see Fig. 3b), which have masses of 1.5 to $6 \times 10^3 M_\odot$ each (Table 3). The most interesting of these complexes is the “rim”, which appears to be wrapped around the ionized emission interacting with it in at least one location called “Region 1”. In this “Region 1”, we find an embedded cluster, a molecular outflow, filaments of H_2 line emission, and an H_2O maser. These phenomena are signs of ongoing (massive) star-forming activity. In at least two other locations of the “ring”, we find signs of such activity, through the presence of water masers, one of which is associated with an H_2 jet. Three regions were observed in a variety of molecular tracers. The LTE molecular masses of these clumps, derived from ^{13}CO -data, are of the order of 330 – $1100 M_\odot$; smaller clumps or cores contained within these regions have several tens of solar masses of molecular gas.

The morphology of the gas associated with Sh 2-217, especially that of the “ring” and “rim”, with their massive clumps and cores, and the signs of past and present star-forming activity contained within it, are all very suggestive of being the result of triggered star formation according to the collect-and-collapse mechanism (cf. Sect. 1).

In the following, we examine the possibility that the material making up the “ring” and “rim” has been swept-up by the expansion of Sh 2-217, and that the cluster of stars embedded in the UCH II region is the consequence of star formation triggered by this expansion. This will be done by looking at the time needed for the expanding ionized gas to reach its present diameter, comparing this to the dynamic age of the UCH II region and the age of the star cluster, and taking into account additional indicators of time, such as the water masers.

The expansion of an H II region is characterized by two phases (Spitzer 1978; Dyson & Williams 1997). We assume that the medium around a massive star is of homogeneous density and temperature. The embedded star begins to ionize the ambient medium; the ionization front moves quickly outwards, and the ionized gas expands rapidly until equilibrium is reached between the number of ionizations and recombinations. At this point, the H II region has reached its so-called Strömgren radius

$$r_{\text{S},0} = \left(\frac{3N_{\text{Lyc}}}{4\pi n_e n_{\text{H}} \alpha} \right)^{1/3}, \quad (3)$$

where n_e and n_{H} are the number densities of electrons and protons, respectively, N_{Lyc} is the number of ionizing photons emitted by the star per second, and $\alpha \approx 2.36 \times 10^{-13} \text{ cm}^3 \text{ s}^{-1}$ is the recombination coefficient (for a kinetic temperature of 8000 K ; Dyson & Williams 1997). This leads to

$$r_{\text{S},0} = 0.3253 \left(\frac{N_{\text{Lyc}}}{10^{48} \text{ s}^{-1}} \right)^{1/3} \left(\frac{10^3 \text{ cm}^{-3}}{n_0} \right)^{2/3} [\text{pc}], \quad (4)$$

where n_0 is the initial particle number density of the ambient neutral gas. If dust is present, a fraction of the UV-photons will be absorbed. If a fraction f_{d} of photons is absorbed, only $(1-f_{\text{d}})N_{\text{Lyc}}$ are available for ionization, and the above equations have to be adjusted likewise. In the phase that follows after this, the expanding gas sends a shock front into the surrounding neutral medium, which precedes the ionization front. In this phase, the radius of the H II region changes with time as

$$r_{\text{S}}(t) = r_{\text{S},0} \left(1 + \frac{7ct}{4r_{\text{S},0}} \right)^{4/7}, \quad (5)$$

where c is the isothermal sound speed in the ionized gas ($c \approx 10 \text{ km s}^{-1}$ at 8000 K ; Spitzer 1978).

Rewriting Eq. (5), we find an expression for the dynamical (expansion) age of the H II region (radii are expressed in pc)

$$t_{\text{dyn}} = 5.587 \cdot 10^{-2} \times r_{\text{S},0} \left[\left(\frac{r_{\text{S},t}}{r_{\text{S},0}} \right)^{7/4} - 1 \right] [\text{Myr}]. \quad (6)$$

In Fig. 23, we show how Eq. (5) describes the change in the radius of the H II region with time, as a function of the density of the ambient medium (indicated by the various labeled curves in each panel), and with the percentage of UV-photons absorbed by dust. Panel a shows the case for no dust, while panels b and c show what happens when respectively 70% and 90% of the ionizing photons from the central star are absorbed by dust. It is clear that it takes a longer time to reach a certain radius when the initial ambient density is higher, and when fewer photons are available for ionization (i.e., when the fraction of photons absorbed by dust is higher). For example, for an initial density of $2 \times 10^3 \text{ cm}^{-3}$ Sh 2-217 would reach its present radius of $\sim 5 \text{ pc}$ in 2.9 Myr , in the absence of dust; for an initial density of $1 \times 10^3 \text{ cm}^{-3}$ this would be only 2.1 Myr . If, on the other hand, 70% of the UV-photons were absorbed by the dust, as suggested by the comparison between the spectral type of the exciting star and the rate of ionizing photons derived from the radio flux (Sect. 4.2), the age of the H II region would be 4.0 Myr for an initial density of $2 \times 10^3 \text{ cm}^{-3}$.

Neutral gas is swept-up by, and collected behind, the shock front. When the mass of swept-up gas reaches a certain mass it starts to fragment, and [massive] stars may form. This process is described by the model developed by Whitworth et al. (1994). The Whitworth et al. analytical model predicts the time at which the fragmentation of the accumulated gas layer begins, the mass (or rather, the column density) of that layer, and the radius of the H II region at that moment. The results depend only weakly on N_{Lyc} , and more strongly on n_0 . An important parameter in the model is the isothermal sound speed in the shocked layer, which Whitworth et al. call “ a_s ”.

The relevant equations of Whitworth et al. (1994) are

$$t_{\text{frag}} = 1.56 \left(\frac{a_s}{0.2} \right)^{7/11} \left[(1-f_{\text{d}}) \frac{N_{\text{Lyc}}}{10^{49}} \right]^{-1/11} \left(\frac{n_0}{10^3} \right)^{-5/11} [\text{Myr}], \quad (7)$$

where t_{frag} is the time at which the fragmentation of the swept-up layer starts. At that moment, the radius of the H II region is

$$r_{\text{frag}} = 5.8 \left(\frac{a_s}{0.2} \right)^{4/11} \left[(1-f_{\text{d}}) \frac{N_{\text{Lyc}}}{10^{49}} \right]^{1/11} \left(\frac{n_0}{10^3} \right)^{-6/11} [\text{pc}], \quad (8)$$

and the mass of the fragments is

$$M_{\text{frag}} = 23.0 \left(\frac{a_s}{0.2} \right)^{40/11} \left[(1-f_{\text{d}}) \frac{N_{\text{Lyc}}}{10^{49}} \right]^{-1/11} \left(\frac{n_0}{10^3} \right)^{-5/11} [M_\odot], \quad (9)$$

where a_s is in km s^{-1} , N_{Lyc} in s^{-1} , and n_0 in cm^{-3} .

We evaluate the above equations for the specific case of Sh 2-217. The exciting star of Sh 2-217 (O9.5 V) has $N_{\text{Lyc}} \approx 1.20 \times 10^{48} \text{ s}^{-1}$, and the radius of the H II region is $\sim 5 \text{ pc}$. Furthermore, our findings in Sect. 4.2 indicate that $f_{\text{d}} = 0.70$.

In Fig. 24, we show the behaviour of various quantities as a function of initial density n_0 and for three values of the sound speed a_s : (a) the timescales t_{dyn} (Sh 2-217), and t_{frag} ; (b) the radius r_{frag} ; and (c) the fragments’ masses M_{frag} . First of all, because we see molecular fragments at the border of Sh 2-217 (viz.

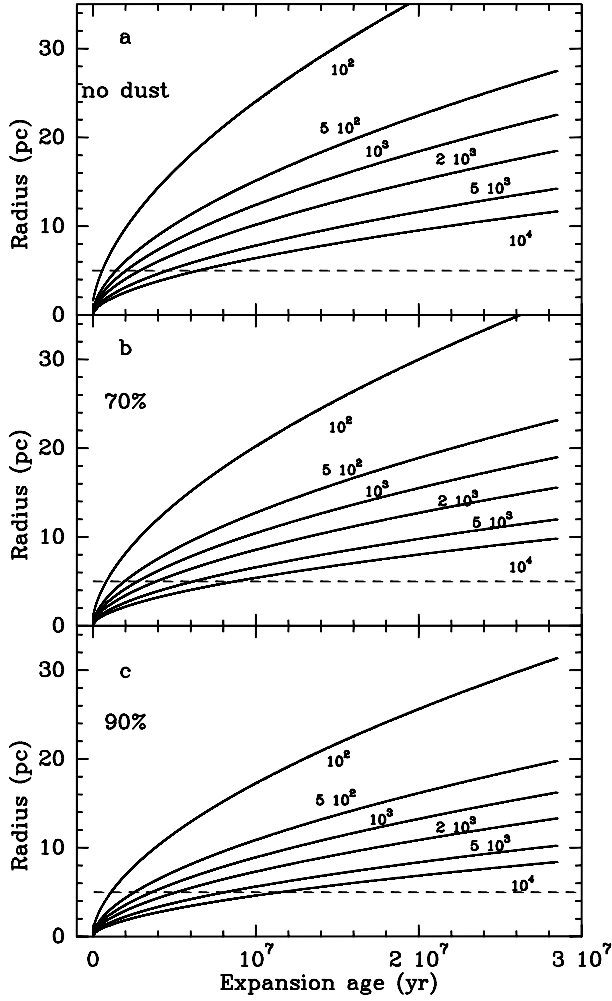


Fig. 23. Radius of Sh 2-217 as a function of time, for various ambient densities and amounts of absorption of UV-photons by dust. We assumed $N_{\text{Ly}\alpha} = 1.20 \times 10^{48} \text{ s}^{-1}$ (O9.5 V star; see Sect. 2). The dashed line indicates the present radius of Sh 2-217. **a)** No dust absorption, all photons are being used for ionization. Curves are for different initial densities of ambient material as labeled. **b)** As **a)**, but for 70% of UV-photons absorbed by dust. **c)** As **a)**, but for 90% absorption by dust.

Regions 1, 2, and 3) it is obvious that $t_{\text{dyn}} > t_{\text{frag}}$. This implies (cf. Fig. 24a) that $n_0 \geq 750 \text{ cm}^{-3}$ ($a_s = 0.2 \text{ km s}^{-1}$), $n_0 \geq 1190 \text{ cm}^{-3}$ ($a_s = 0.4 \text{ km s}^{-1}$), and $n_0 \geq 1550 \text{ cm}^{-3}$ ($a_s = 0.6 \text{ km s}^{-1}$). Likewise, the present radius of the H II region must be larger than the radius at which fragmentation starts. From Fig. 24b, we see that this implies minimum values for n_0 of 760, 1200, and 1580 cm^{-3} for $a_s = 0.2, 0.4,$ and 0.6 km s^{-1} , respectively. Finally, Fig. 24c shows that to find masses of the fragments similar to those we detect, values of $0.4 < a_s < 0.6 \text{ km s}^{-1}$ are required.

If we now assume that $n_0 = 2000 \text{ cm}^{-3}$, Fig. 24 shows that the expansion age of Sh 2-217 is 4.0 Myr. Fragmentation starts after 2.4, 2.8, and 3.1 Myr, for $a_s = 0.4, 0.5,$ and 0.6 km s^{-1} , respectively. This is 1.6 Myr ($a_s = 0.4 \text{ km s}^{-1}$), 1.2 Myr ($a_s = 0.5 \text{ km s}^{-1}$), and 0.9 Myr ($a_s = 0.6 \text{ km s}^{-1}$) ago. The masses of the fragments were then $\sim 280, 635,$ and $1235 M_{\odot}$, for $a_s = 0.4, 0.5,$ and 0.6 km s^{-1} , respectively. The last mass value lies close to what we find for the mass of “Region 1” from the ^{13}CO -data ($\sim 1100 M_{\odot}$; Sect. 4.3.1). The model predicts that this fragment was formed 0.9–1.2 Myr ago ($a_s = 0.6$ – 0.5).

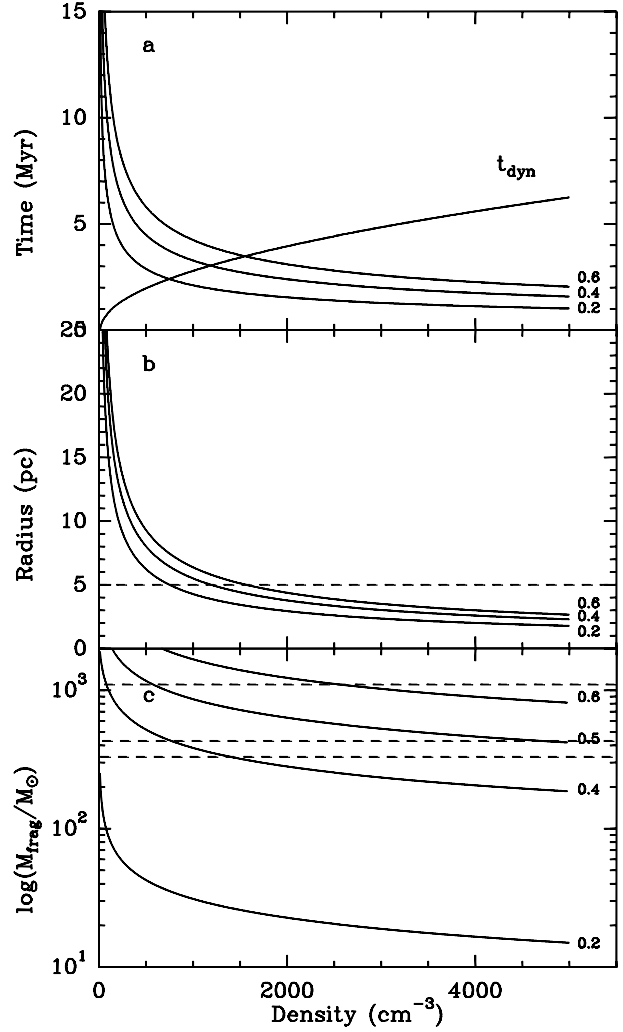


Fig. 24. Results of the Whitworth et al. (1994) model for the conditions in Sh 2-217, using the equations given in the text. We assumed $N_{\text{Ly}\alpha} = 1.20 \times 10^{48} \text{ s}^{-1}$, that 70% of the ionizing photons are absorbed by dust, and that the present radius of the H II region is 5 pc. The different panels show the variation of various physical quantities as a function of the initial density of the ambient neutral medium, n_0 . **a)** Time. The curve labeled t_{dyn} shows the expansion age of Sh 2-217, needed to reach its actual radius. The other curves show t_{frag} , the time at which fragmentation starts. Three values of the sound speed are indicated. **b)** As **a)**, but for the radius of Sh 2-217 at which fragmentation starts. The dashed line indicates the actual radius of Sh 2-217. **c)** As **a)**, but for the masses of the fragments. An additional curve, for sound speed $a_s = 0.5 \text{ km s}^{-1}$, is drawn in. The three dashed lines indicate the masses (derived from ^{13}CO data) of the three “Regions” mapped in more detail (see Fig. 3b).

In one of the molecular fragments, “Region 1”, a star cluster has formed, and one or more of its stars has given rise to an UCH II region. We now have to ask whether there has been enough time for this to occur. In Sect. 4.6, we concluded that the cluster of stars at the border of Sh 2-217 most likely has an age of ≤ 1 Myr, Porras et al. (2000) having derived 0.3 Myr. A young age for the cluster is corroborated by the presence of an UCH II region and an H_2O maser (Sect. 4.5). Water masers occur in the first 10^4 yrs of the lifetime of a massive star (Breen et al. 2010, their Fig. 6). The exciting star of the UCH II region is of type B0 V ($18 M_{\odot}$, Stahler & Palla 2004); the time needed for such a star to form is \leq a few 10^5 yrs. As soon as it reaches the main-sequence, it will not yet have reached its final

mass. While accretion continues, the star will nevertheless start to produce ionizing photons. However, at sufficiently high accretion rates, the formation of an H II region may be inhibited, or at least limited to a small volume close to the stellar surface (e.g., Walmsley 1995). This may delay the onset of an (expanding) H II region for a few 10^3 yrs, which is a negligible amount in our present order-of-magnitude calculation.

From the NVVS radio data, we derive a beam-corrected radius of the UCH II region of about 0.9 pc (this corresponds to the radius of the lowest closed 1.4 GHz contour that surrounds the region). This value is consistent with the beam-corrected radius at the 5σ level of the MSX A ($8 \mu\text{m}$) emission associated with the UCH II region. From a comparison of the output of the rate of Lyman-continuum photons emitted by the exciting star, and the radio continuum flux, we found that about 90% of these photons are not used for ionization, i.e. are likely to have been absorbed by dust. The core of the “Region 1” fragment has a radius of about 0.5 pc and a mass of about $100 M_{\odot}$; this translates into a number density of about $5 \times 10^3 \text{ cm}^{-3}$. Assuming therefore that for the UCH II region $n_0 = 5000 \text{ cm}^{-3}$, Eqs. (4) and (6) tell us that in order to reach its present radius of 0.9 pc, its dynamical (expansion) age is about 0.53 Myr. For $n_0 = 3000, 2000 \text{ cm}^{-3}$ the expansion ages are 0.41 Myr and 0.33 Myr, respectively.

The age of the star cluster (≤ 1 Myr) and the dynamical age of the UCH II region (~ 0.3 – 0.5 Myr, depending on the initial density) add up to ≤ 1.3 – 1.5 Myr. Taking into consideration that this upper limit is likely to be even lower, because the UCH II region probably formed and started expanding before the cluster reached its present age, this time interval is entirely consistent with the times for the onset of fragmentation derived above for “Region 1” (0.9–1.2 Myr ago, for $a_s = 0.6, 0.5 \text{ km s}^{-1}$, respectively). Thus, application of this relatively simple model shows that the ages, masses, and sizes of the various constituents (Sh 2-217, the UCH II region, and their exciting stars, the molecular fragments in the “ring” and “rim”, the star cluster, and the masers) in this region are consistent with an interpretation of sequential star formation. The Whitworth et al. (1994) model is unrealistic in that it assumes expansion in a homogeneous, spherically symmetric medium that is several pc across; in reality, the medium is likely to be clumpy and (as in this case) morphologically-challenged. However, the indication it gives that in Sh 2-217 we may see the collect-and-collapse mechanism at work, is trustworthy to first order.

5.1. The influence of N_{Lyc}

In our analysis of the ionized gas (Sect. 4.2) and in the discussion above, we have taken the number of Lyman continuum photon emitted by the exciting stars from Panagia (1973). Since that publication, new calibrations for early-type stars have become available, and one may ask how our results might change had we used more recent values. The (perhaps surprising) result is that they do not.

According to Martins et al. (2005), the exciting star of Sh 2-217 (O9.5 V) has $N_{\text{Lyc}} = 3.63 \times 10^{47} \text{ s}^{-1}$ (28% of the Panagia 1973 value), the same as what we derive from the radio continuum data. Hence virtually all Lyman-continuum photons would be used for ionization, and $f_d \approx 0$ (cf. Sect. 5). Redoing the calculations, using the same estimate of the initial density, we find that the dynamical age of Sh 2-217 (i.e., the time needed to reach its present radius) is 3.94 Myr. With Panagia’s value of N_{Lyc} this was 3.95 Myr (which we rounded off to 4.0 Myr in Sect. 5). The times at which fragmentation sets in (for the various values of a_s) and the masses of the fragments, are also both the

same. The reason for this is that one always has the same number of photons used to ionize the gas, namely that derived from the radio continuum data, which is equal to $N_{\text{Lyc}} \times (1 - f_d)$: if the star has a high output of photons (as in Panagia 1973), we find that many are absorbed by dust or directly escape from the H II region; if the star has a lower output (as in the Martins et al. 2005 calibration), then almost all of them are used to ionize. In both cases, $N_{\text{Lyc}} \times (1 - f_d)$ is the same.

The same thing is of course found for the UCH II region, when using $N_{\text{Lyc}} = 2.51 \times 10^{47} \text{ s}^{-1}$ (Smith et al. 2002). In this case, $f_d = 0.84$ (was 0.90) and the dynamical ages for the various values of the initial density are found to be the same as before.

Acknowledgements. The research presented in this paper is based in part on observations with the Medicina 32-m telescope operated by INAF-Istituto di Radioastronomia, and on observations made with the Italian Telescopio Nazionale Galileo (TNG). The TNG is operated on the island of La Palma by the Fundación Galileo Galilei of the INAF (Istituto Nazionale di Astrofisica) at the Spanish Observatorio del Roque de los Muchachos of the Instituto de Astrofísica de Canarias.

We have made use of data from the Canadian Galactic Plane Survey, a Canadian project with international partners, supported by the Natural Sciences and Engineering Council. We have furthermore used NASA’s Astrophysics Data System Bibliographic Services (ADS) and the SIMBAD database, operated at CDS, Strasbourg, France.

J.B. and F.M. strongly protest the shameless, continuing dismantling of scientific research by a succession of Italian governments, especially the present one.

References

- Allen, C. W. 1976, *Astrophysical Quantities*, 3rd edn. (London: Athlone press)
- Baffa, C., Comoretto, G., Gennari, S., et al. 2001, *A&A*, 378, 722
- Blake, G. A., Sutton, E. C., Masson, C. R., & Phillips, T. G. 1987, *ApJ*, 315, 621
- Brand, J., & Blitz, L. 1993, *A&A*, 275, 67
- Brand, J., & Wouterloot, J. G. A. 1998, *A&A*, 337, 539
- Breen, S. L., Ellingsen, S. P., Caswell, J. L., & Lewis, B. E. 2010, *MNRAS*, 401, 2219
- Codella, C., & Felli, M. 1995, *A&A*, 302, 521
- Codella, C., Felli, M., & Natale, V. 1996, *A&A*, 311, 971
- Condon, J. J., Cotton, W. D., Greisen, E. W., et al. 1998, *AJ*, 115, 1693
- Deharveng, L., Lefloch, B., Zavagno, A., et al. 2003a, *A&A*, 408, L25
- Deharveng, L., Zavagno, A., Salas L., et al. 2003b, *A&A*, 399, 1135
- Deharveng, L., Zavagno, A., Caplan, J. 2005, *A&A*, 433, 565
- Deharveng, L., Lefloch, B., Massi, F., et al. 2006, *A&A*, 458, 191
- Deharveng, L., Lefloch, B., Kurtz, S., et al. 2008, *A&A*, 482, 585
- Deharveng, L., Zavagno, A., Schuller, F., et al. 2009, *A&A*, 496, 177
- Dickman, R. L., & Clemens, D. P. 1983, *ApJ*, 271, 143
- Dyson, J. E., & Williams, D. A. 1997, *The Physics of the Interstellar Medium*, 2nd edn. (IOP Publ. Ltd)
- Egan, M. P., Price, S. D., Moshir, M. M., et al. 1999, *The Midcourse Space Experiment Point Source Catalog version 1.2*, Explanatory Guide, AFRL-VS-TR-1999-1522, Air Force Research Laboratory
- Elmegreen, B. G. 1998, in *Origins*, ed. C. E. Woodward, J. M. Shull, & H. A. Thronson, ASP Conf. Ser., 148, 150
- Elmegreen, B. G., & Lada, C. J. 1977, *ApJ*, 214, 725
- Fich, M., Treffers, R. R., & Dahl, G. P. 1990, *AJ*, 99, 622
- Frerking, M. A., Langer, W. D., & Wilson, R. W. 1982, *ApJ*, 262, 590
- Furuya, R. S., Kitamura, Y., Wootten, A., Claussen, M. J., & Kawabe, R. 2001, *ApJ*, 559, L143; Erratum: 2007, *ApJ*, 659, L81
- Furuya, R. S., Kitamura, Y., Wootten, A., Claussen, M. J., & Kawabe, R. 2003, *ApJS*, 144, 71; Erratum: 2007, *ApJS*, 171, 349
- Georgelin, Y. M., Georgelin, Y. P., & Roux, S. 1973, *A&A*, 25, 337
- Huang, Y.-L., & Thaddeus, P. 1986, *ApJ*, 309, 804
- Hillenbrand, L. A. 2008, in *A decade of extrasolar planets around normal stars*, ed. M. Livio, K. Sahu, & J. Valenti (Cambridge Univ. Press), 84
- Jackson, P. D., & Sewall, J. R. 1982, in *Regions of recent star formation*, ed. R. S. Roger, & P. E. Dewdney (Dordrecht: Reidel), 221
- Koornneef, J. 1983, *A&A*, 128, 84
- Kramer, C. 1988, *Diplomarbeit*, I. Phys. Inst., Univ. Köln.
- Kramer C., & Winnewisser, G. 1991, *A&AS*, 89, 421
- Lee, H.-T., Chen, W. P., Zhang, Z.-W., & Hu, J.-Y. 2005, *ApJ*, 624, 808
- Leistra, A., Cotera, A. S., & Liebert, J. 2006, *AJ*, 131, 2571

- Levreault, R. M. 1988, *ApJS*, 67, 283
- MacLaren, I., Richardson, K. M., & Wolfendale, A. W. 1988, *ApJ*, 333, 821
- Martins, F., & Plez, B. 2006, *A&A*, 457, 637
- Martins, F., Schaerer, D., & Hillier, D. J. 2005, *A&A*, 436, 1049
- Matsakis, D. N., Evans, N. J., II, Sato, T., & Zuckerman, B. 1976, *AJ*, 81, 172; Erratum: 1976, *AJ*, 81, 1004
- Moffat, A. F. J., Fitzgerald, M. P., & Jackson, P. D. 1979, *A&AS*, 38, 197
- Ott, M., Witzel, A., Quirrenbach, A., Krichbaum, et al. 1994, *A&A*, 284, 331
- Palla, F., & Stahler, S. W. 1999, *ApJ*, 525, 772
- Panagia, N. 1973, *AJ*, 78, 929
- Pomarès, M., Zavagno, A., Deharveng, L., et al. 2009, *A&A*, 494, 987
- Porras, A., Cruz-González I., & Salas, L. 2000, in *Star Formation from the Low to the Large Scale*, ed. F. Favata, A. Kaas, & A. Wilson (Noordwijk: ESA SP-445), 491
- Reach, W. T., Rho, J., Young, E., et al. 2004, *ApJS*, 154, 385
- Reed, C. 1998, *ApJS*, 115, 271
- Reipurth, B. 1983, *A&A*, 117, 183
- Rieke, G. H., & Lebofsky, M. J. 1985, *ApJ*, 288, 618
- Roger, R. S., & Leahy, D. A. 1993, *AJ*, 106, 31
- Rohlfs, K., & Wilson, T. L. 1996, *Tools of Radio Astronomy*, 2nd edn. (Berlin: Springer Verlag)
- Russeil, D., Adami, C., & Georgelin, Y. M. 2007, *A&A*, 470, 161
- Scalo, J. 1998, in *The Stellar Initial Mass Function*, ed. G. Gilmore, & D. Howell, ASP Conf. Ser., 142, 201
- Schuster, K.-F., Boucher, C., Brunswig, W., et al. 2004, *A&A*, 423, 1171
- Smith, L. J., Norris, R. P. F., & Crowther, P. A. 2002, *MNRAS*, 337, 1309
- Spitzer, L. 1978, *Physical Processes in the Interstellar Medium* (Wiley & Sons)
- Stahler, S. W., & Palla, F. 2004, *The Formation of Stars* (Wiley)
- Stetson, P. B. 1987, *PASP*, 99, 191
- Strong, A. W., & Mattox, J. R. 1996, *A&A*, 308, L21
- Taylor, A. R., Gibson, S. J., Peracaula, M., et al. 2003, *AJ*, 125, 3145
- Testi, L., Palla, F., Prusti T., Natta, A., & Maltagliati, S. 1997, *A&A*, 320, 159
- Tokunaga, A. T., & Vacca, W. D. 2005, *PASP* 117, 421
- Valdettaro, R., Migenes, V., Trinidad, M. A., Brand, J., & Palla, F. 2008, *ApJ*, 675, 1352
- Van Dishoeck, E. F., Blake, G. A., Draine, B. T., & Lunine, J. I. 1993, in *Protostars and Planets III*, ed. E.H. Levy & J.I. Lunine (Univ. of Arizona Press), 163
- Walmsley, C. M. 1995, *Rev. Mex. Astron. Astrofis. Ser. Conf.*, 1, 137
- Whitworth, A. P., Bhattal, A. S., Chapman, S. J., Disney, M. J., & Turner, J. A. 1994, *MNRAS*, 268, 291
- Zavagno, A., Deharveng, L., Comeron, F., et al. 2006, *A&A*, 446, 171
- Zavagno, A., Russeil, D., Motte, F., et al. 2010, *A&A*, 518, L81
- Zhou, S., Evans, N. J., Güsten, et al. 1991, *ApJ*, 372, 518